

UNIVERSITÀ DEGLI STUDI DI MESSINA

Dipartimento di Scienze Biomediche, Odontoiatriche

e delle Immagini Morfologiche e Funzionali

CORSO DI DOTTORATO IN BIOINGEGNERIA APPLICATA ALLE SCIENZE MEDICHE

XXXV CICLO – MED/36



COMPREHENSIVE ASSESSMENT OF VIRTUAL MONOENERGETIC IMAGING FOR CORONARY COMPUTED TOMOGRAPHY ANGIOGRAPHY

Tutor:

Chiar.mo Prof. Michele GAETA

Tesi di dottorato di:

Dott. Tommaso D'ANGELO

509035

ANNO ACCADEMICO 2021/2022

INDEX

INTRODUCTION	- 1 -
1. BASIC PRINCIPLES OF COMPUTED TOMOGRAPHY	- 3 -
1.1. Basic physical principles	- 3 -
1.2. From Multi-detector to Dual-source CT	- 5 -
2. DUAL-ENERGY CT	- 7 -
2.1. Basic principles of dual-energy CT	- 7 -
2.2. Technical approaches to dual-energy CT	- 8 -
2.2.1. Dual-Source	- 9 -
2.2.2. Dual-Layer	- 9 -
2.2.3. Sequential acquisition	- 10 -
2.2.4. Rapid kVp switching	- 10 -
3. CORONARY CT ANGIOGRAPHY	- 11 -
3.1. Evolution of CCTA in the assessment of coronary artery disease	- 11 -
3.2. Segmental anatomy of coronary arteries	- 13 -
4. DUAL-ENERGY IMAGING AND CORONARY CTA	- 15 -
4.1. Image quality assessment	- 15 -
4.1.1. Objective image quality parameters	- 16 -
4.1.2. Subjective image assessment	- 17 -
4.2. Improving image quality	- 18 -
4.3. Low-dose contrast media protocols	- 19 -
4.4. Assessing stent patency	- 20 -
4.5. Virtual non-contrast images for coronary calcium scan	- 20 -
5. IMPROVED CORONARY ARTERY CONTRAST ENHANCEMENT USING NOISE-OPTIMISED VIRTUAL MONOENERGETIC IMAGING FROM DUAL-SOURCE DUAL-ENERGY CT	- 21 -
5.1. Background	- 21 -
5.2. Methods	- 22 -
5.2.1. Patient selection	- 22 -
5.2.2. DECT image acquisition	- 23 -
5.2.3. DECT image reconstruction	- 24 -
5.2.4. Objective image analysis	- 25 -

5.2.5. Subjective image analysis.....	25 -
5.2.6. Statistical analysis.....	26 -
5.3. Results.....	27 -
5.3.1. Study population.....	27 -
5.3.2. Objective image analysis	28 -
5.3.3. Subjective image analysis.....	30 -
5.4. Discussion.....	31 -
6. IMPROVED CORONARY ARTERY CONTRAST ENHANCEMENT USING VIRTUAL MONOENERGETIC IMAGING FROM DUAL-LAYER SPECTRAL DETECTOR CT	35 -
6.1. Background.....	35 -
6.2. Methods	36 -
6.2.1. Study population.....	36 -
6.2.2. DECT acquisition protocol	37 -
6.2.3. Image reconstruction	38 -
6.2.4. Objective image quality analysis	38 -
6.2.5. Subjective image assessment.....	39 -
6.2.6. Coronary stenosis assessment.....	39 -
6.2.7. Statistical analysis.....	40 -
6.3. Results.....	41 -
6.3.1. Study population.....	41 -
6.3.2. Objective image quality analysis	41 -
6.3.3. Subjective image assessment.....	44 -
6.3.4. Coronary stenosis assessment.....	46 -
6.4. Discussion.....	49 -

INTRODUCTION

Coronary computed tomography angiography (CCTA) is a technique that allows for a non-invasive evaluation of anatomy, structure and function of the heart, as well as of coronary arterial patency.

It consists of a contrast-enhanced computed tomography of the thorax, which is synchronized with the patient's electrocardiographic activity that permits to acquire high-resolution images of the heart and coronary arteries. Each vessel can be assessed with specific reconstructions in order to better assess the presence of stenoses.

Conversely to coronary angiograms, CCTA images also allow for extraluminal evaluation of coronary vessels, as well as for plaque and perivascular space analysis, providing a complete morphological picture of coronary atherosclerosis.

Currently, this technique is considered the first-line non-invasive test for the diagnostic workup of patients with low or intermediate risk of coronary artery disease (CAD) and chest pain, according to the guidelines of the European Society of Cardiology of 2019.¹

Thanks to the speed and ease of execution and the increasing availability, CCTA has rapidly become a widespread examination in radiologists' clinical routine.

During the last two decades, CCTA has also benefited of the technological advances in computed tomography imaging. In particular, its diagnostic value has been further expanded by the application of dual-energy computed tomography (DECT) techniques.²

DECT is based on the simultaneous acquisition of X-ray beams with two different energy levels. Since each tissue shows a different attenuation profile when exposed to different

energy levels, DECT can provide quantitative information about material composition. This may allow to differentiate structures with similar attenuation in conventional CT.³

There are different technical approaches to obtain DECT images, which can be easily differentiated in single-source, dual-source, and dual-layer systems.²

One of the unique features of DECT is the possibility to obtain virtual monoenergetic images at different keV levels.⁴

This algorithm has demonstrated to provide clear advantages in DE-CCTA. Previous studies have shown that low-keV monoenergetic reconstructions increase iodine attenuation and contrast, whereas high-keV monoenergetic reconstructions can reduce beam-hardening artefacts.⁴

The purpose of our research is to prove that CCTA monoenergetic reconstructions obtained from dual-source (DSCT) and dual-layer (DLCT) platforms show improved objective and subjective image quality compared to conventional images.

1. BASIC PRINCIPLES OF COMPUTED TOMOGRAPHY

Computed tomography (CT) allows to acquire images of inorganic and organic materials from the meters down to the tens of nanometers length scales. One of the main advantages provided by CT is that the technique provides a non-destructive analysis of materials.

The first medical CT scan was performed in September 1971 by Sir Godfrey Hounsfield, who won the Nobel Prize in Medicine in 1979 to have developed the theoretical underpinnings of computed tomography.⁵ In the next five decades, CT scanners have become wide available for the clinical use. The technology improved, with an increasingly better spatial and temporal resolution, and with a reduction of the acquisition time.

Nowadays, CT represents a fundamental tool for physicians. As a proof of concept, about 62 million CT scans were obtained each year in the early twenty-first century in the United States, compared with about 3 million in 1980.⁶

1.1. Basic physical principles

CT systems translate the attenuated radiation collected by a system of detectors into gray-scale values. The attenuation results when the X-ray beam passes through a material, and it is either absorbed or scattered differently depending on X-ray beam energy level and on the nature of the irradiated material.

Microscopically, two main effects contribute to the attenuation of materials⁷ (Figure 1):

- **photoelectric effect** (Fig. 1A) consists of the ejection of an electron from the innermost shell of an atom (K-shell) by an incident photon. The void is filled from an electron of an adjacent shell, causing the release of a photoelectron.
- **Compton effect** or **Compton scattering** (Fig. 1B) is proportional to the electron density. It becomes the dominant process when human tissues are irradiated between 30 keV and 30 MeV, a range used in medical applications for both diagnostic and therapeutic purposes. In Compton effect, photons interact with electrons of the outermost atomic shell.

Another phenomenon, called **Reyleigh scattering**, occurs mainly with very low energy X-rays (15-30 keV). This type of interaction has a low probability of occurrence in the diagnostic energy range.

On the other hand, the **pair production** phenomenon does not become significant unless the energy exceeds a minimum of 1.02 MeV. Moreover, its probability increases for elements with high atomic number. Therefore, it has no particular importance for soft tissues at low energy levels, as occurs in the medical setting.

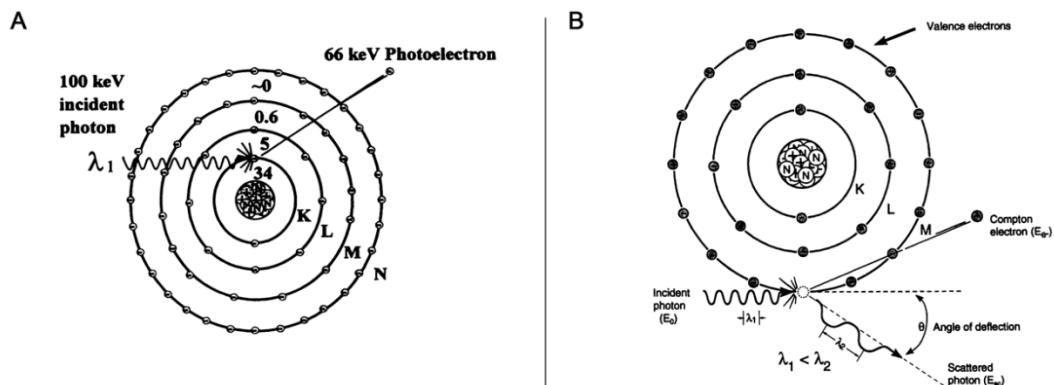


Figure 1. Schematic representations of the photoelectric (A) and Compton (B) effects. Adapted from Bushberg J., et al.⁷

In CT imaging, multiple acquisitions at different angles are performed thanks to a rotation of the system in order to spatially compute X-ray attenuation coefficients. Modern platforms perform about 1,000 projections in a full 360 degrees rotation.⁸

Furthermore, it's possible to acquire multiple slices across an object by the translation of a narrow X-ray beam and its detector, or a broader beam and multiple detector elements across the object.

The final degree of attenuation of a certain volume of a tissue undergoing a 120 kVp X-ray source can be measured in a numerical scale expressed in **Hounsfield Units (HU)**. On this scale, we arbitrarily assign a value of 0 to water. All other values aren't absolute but relative to water. The lowest value is assigned to air and calibrated to absolute black in a gray scale; a higher value than water is assigned to dense objects such as calcium, metal or contrast media. This scale allows tissues with different density to be displayed differently in the final image.

1.2. From Multi-detector to Dual-source CT

Since the introduction of second-generation CT systems, the fan-shaped beam required more coverage to be detected. For this reason, it became necessary to use an array of detectors (up to 30). As a consequence, scan time was reduced to less than 20 seconds.⁸

Third generation CT systems have benefited of the introduction of multi-detector rows that extend coverage along the z-axis. With the use of third-generation multi-detector CT entire anatomical regions, such as thorax or abdomen, can be examined within one breath-hold with a single rotation of the system. This also made ECG-gated computed tomography of the heart possible.^{9,10}

In the last decades gantries could rotate in less than 0.3 seconds, and this allowed to perform fast examinations such as coronary CT angiography. Wintersperger et al. demonstrated that it was possible to perform ECG-gated cardiac scanning with a good diagnostic quality using a 64-slice CT platform with a gantry rotation time of 0.33 s.¹¹ However, in order to further improve temporal resolution CT platforms with two X-ray tubes installed with a 90° offset angle were introduced.

This technological advance allowed to split the scan into two half-scans by each tube, increasing the temporal resolution up to 75ms and overcoming image quality concerns at higher heart rate.⁸ In addition, this allowed for other potential applications, such as the fast scanning of uncooperative patients or pediatric patients.

However, one of the main disadvantages in these platforms is the so called "cross-scatter radiation" phenomenon that occurs because the radiation beam can partially hit the noncorresponding detector. Finally, each tube can be operated at different voltages, allowing to acquire dual-energy data (*Dual-Energy CT, see below*).

2. DUAL-ENERGY CT

Conventionally, CT characterization of material relies on the different elemental attenuation. As mentioned above, the attenuation is mainly a result of Compton scattering and photoelectric effect, and it depends on the mass density of the material and the photon energy.

However, differentiating contrast media from different tissues with similar attenuation can be challenging. In particular, contrast enhancement can only be assessed indirectly, by differences in attenuation, since it may not be possible to distinguish iodine from other high-density materials. In fact, measuring iodine enhancement by tissue attenuation does not directly reflect the amount of iodine in that tissue and it is influenced by the intrinsic attenuation of the tissue.

Dual-energy CT allows to overcome these limitations and improve the clinical and diagnostic usefulness of computed tomography.

2.1. Basic principles of dual-energy CT

The concept of dual-energy CT derives from using a second X-ray spectrum with a different energy (dual-energy) that allows to obtain additional attenuation measurements, in order to aim at differentiating materials.

In general, tissues with different composition respond differently to X-rays at various energy levels. Using the known differences between the attenuation spectra of each element, it is possible to quantify and differentiate material composition in tissues.

This is possible thanks to *k-edge* (Figure), which describes the specific attenuation increase that occurs when the X-ray energy level overcomes the K-shell binding energy

of an element, which is specific and directly proportional to the atomic number of an element.

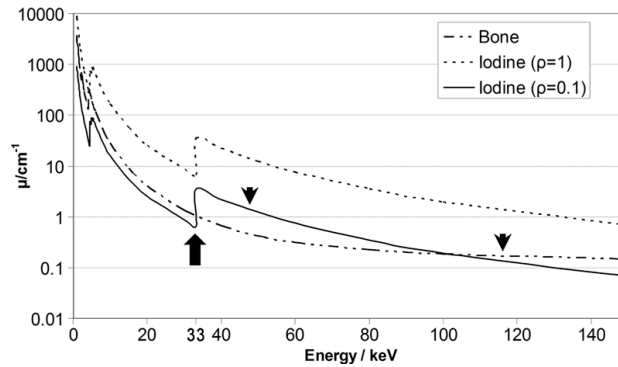


Figure 2. Linear attenuation coefficients for bone, iodine (with 1 g/cm^3 density) and iodine with lower density ($\rho = 0.1 \text{ g/cm}^3$) as a function of energy expressed in kiloelectron volts. Measuring attenuation at least two different energy levels (arrowheads) allows to differentiate the two materials. K-edge for iodine is set at 33 KeV (arrow).

Contrast media used in clinical routine such as iodine and barium have K-shell binding energies of 33 keV and 37 keV respectively, therefore their attenuation increases for energy level just above these values, which are in the range of those used for diagnostic purposes.¹²

Obtaining datasets with spectral information is the aim of dual-energy CT and these can be post-processed into different types of images: iodine density images, virtual non-contrast images, effective atomic number (Z-effective), monoenergetic images (MonoE), or reconstructions that selectively enhance/remove uric acid. These post-processing algorithms allows CT to become a multiparametric examination, which is not merely based on attenuation differences of materials.

2.2. Technical approaches to dual-energy CT

Dual-energy CT platforms have different technology which is based on different technical approaches.

2.2.1. Dual-Source

The first DECT platforms used in clinical routine are the so-called **Dual-Source CT** (DSCT) scanners.

They consist of two tubes at different voltages with detectors mounted orthogonally in the same gantry.

The technique eliminates the delay between the two acquisitions, because the data are acquired simultaneously. These systems keep the disadvantages of the higher radiation exposure. Moreover, a phenomenon called "cross-scatter radiation" can occur because the radiation beam can partially hit the noncorresponding detector. Different generations of DSCT scanners have been developed for the last 15 years, that optimized image quality and radiation dose exposure.

2.2.2. Dual-Layer

This technological approach takes advantage of the ability of the detector to separate a polychromatic spectrum of X-rays in two different energy spectra. This ability derives from the two layers that compose the detector, which are made by different materials, allowing for decomposition of the polychromatic spectrum. In particular, the bottom layer (gadolinium oxysulphide) selectively detects high-energy photons, while the top layer (yttrium) selectively detects low-energy photons.

The main advantage of Dual-Layer CT systems is that the low- and high-energy projections are simultaneously acquired, and data are always recorded from both layers in spectral datasets.

2.2.3. Sequential acquisition

This approach requires the least technological effort, since it consists of sequential acquisition at different tube voltages. However, the time delay between the two acquisitions leads to motion artifacts of organs such as heart or lungs. Some systems may implement software motion correction but this approach determines a higher radiation dose exposure. However, the technique is effective for the characterization of stationary material such as kidney stones, metal structures or foreign bodies.

2.2.4. Rapid kVp switching

This technique consists of rapid switching of X-ray tube potential. It requires a very fast transition time from low to high potential, and an equally fast data sampling time. The gantry rotation time is increased to allow the additional acquisitions, prolonging the time required to complete the scan and increasing the radiation exposure. Moreover, low-KeV projections show an increased noise because of the lower penetration of X-rays.

3. CORONARY CT ANGIOGRAPHY

Coronary-CTA has been accepted as one of the main non-invasive tests for the management of patients with suspected coronary artery disease (CAD). The European Society of Cardiology, in 2019, recommended the use of CCTA for the assessment of chronic coronary syndromes in patients with low risk of CAD and chest pain¹. However, this technique shows considerable potential for future applications thanks to its ability for tissue characterization together with its increasing availability for clinical use.

3.1. Evolution of CCTA in the assessment of coronary artery disease

In the past, one of the major technical problems in acquiring computed tomography images of the heart was the high temporal resolution needed to avoid motion artifacts of the organ. Ironically, the technical feasibility of studying coronary arteries with magnetic resonance was described prior to CT. In 1993 a study described a MRI technique to assess the patency of coronary arteries.¹³

The first technology that made it possible to produce CT images of the coronary arteries was the **electron beam computed tomography** (EBCT). This system offered a higher temporal resolution because the tube isn't rotated mechanically, instead the electron-beam focal point is swept electronically. In 1998, an initial study compared coronary angiography with EBCT in 125 patients. Due to technical limitations, only proximal and mid segments could be evaluated. Researchers reported a considerable sensitivity (92%) and specificity (94%). The results were noteworthy, although they doesn't take into account the not evaluable segments and the high image noise.¹⁴

The introduction of **multi-detector CT** (MDCT) systems with "slip-ring" technology made it possible to scan whole parts of the body within one breath-hold in the same

rotation of the system. Hence, thanks to the higher temporal and spatial resolution, it became possible to see small non-stationary structures such as coronary arteries. In 2008, an international study, called CORE-64, examined the accuracy of MDCT angiography as compared with conventional angiography. The study revealed a specificity of 80% and a sensitivity of 85%, with a good correlation in disease severity assessment ($r=0.81$).¹⁵

The results from two recent studies, the SCOT-HEART trial (Scottish Computed Tomography of the Heart) and the PROMISE trial (Prospective Multicenter Imaging Study for Evaluation of Chest Pain) assessed the role of CCTA in the diagnostic strategy for low- to intermediate-risk patients with suspicion of obstructive CAD.

The SCOT-HEART trial shows that the use of CCTA as a first approach (as compared with standard care) leads to earlier initiation of preventive therapy with a significant 41% reduction in non-fatal and fatal myocardial infarction ($p = 0.004$) at 4.8 years. Although CCTA was associated with a higher number of short-term coronary revascularization, there was no difference in revascularization at 5 years, as a probable result of early medical therapy.

The larger PROMISE trial randomly assigned 10003 patients requiring evaluation for angina due to suspected CAD to either functional stress testing or CCTA. CCTA did not improve the incidence of nonfatal MI, hospitalization for unstable angina, all-cause death, and major procedural complications, in comparison with functional testing. However, since CCTA can detect nonobstructive coronary artery disease, this resulted in an ability in predicting events which was better than functional testing. Moreover CAD-RADS, a standardized findings communication method for the reporting of CCTA exams, had better prognostic value at predicting MACEs compared with coronary artery calcium scoring or ASCVD risk calculation.

If analyzed together, both trials have proven the role of CCTA in management of patients with stable chest pain and a low- to intermediate risk of CAD. If the patient is eligible for both functional and anatomic testing, important clinical information can be obtained through both methods. Moreover, if the first test, anatomical or functional, does not provide diagnostic images, it is possible to evaluate the execution of the remaining tests, including CCTA, before the invasive approach. Furthermore, it has been proven that patients' knowledge of the presence of plaque, demonstrable only with anatomical testing, helps starting a therapeutic strategy earlier.

Such evidences led to the inclusion of CCTA both in the 2019 ESC guidelines on Chronic Coronary Syndromes¹ (Figure) and in the 2021 AHA guidelines for the Evaluation and Diagnosis of Chest Pain.¹⁶

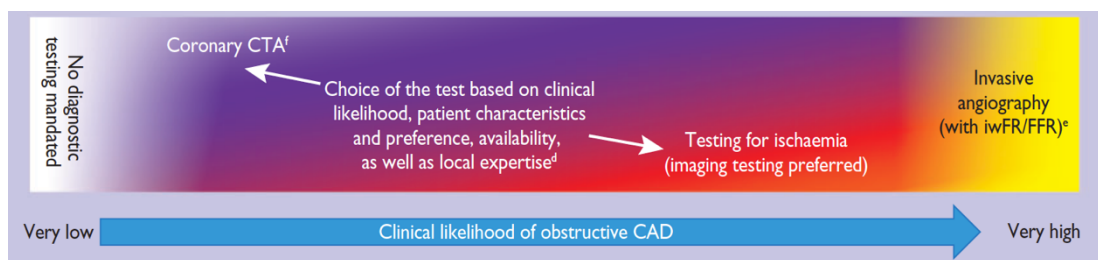


Figure 3. Diagnostic tests offered for the management of patients with suspected CAD. The choice is based on the clinical likelihood of obstructive CAD. In patient with low risk, coronary CTA represents the main test that should be performed. From Knuuti, J, et al. ¹

3.2. Segmental anatomy of coronary arteries

The segmental analysis of coronary arteries has been originally described in 1975 by the American Heart Association and the Council on Cardiovascular Surgery with a standardized Reporting System for patients with CAD (Figure 4). This is the model currently in use.¹⁷

The model is mainly based on conventional angiographic images of the coronary arteries; however, it can be easily adapted to other anatomic techniques. Adherence to the proposed scheme is essential in the communication between the physician and the radiologist to ensure standardization and reproducibility of results.

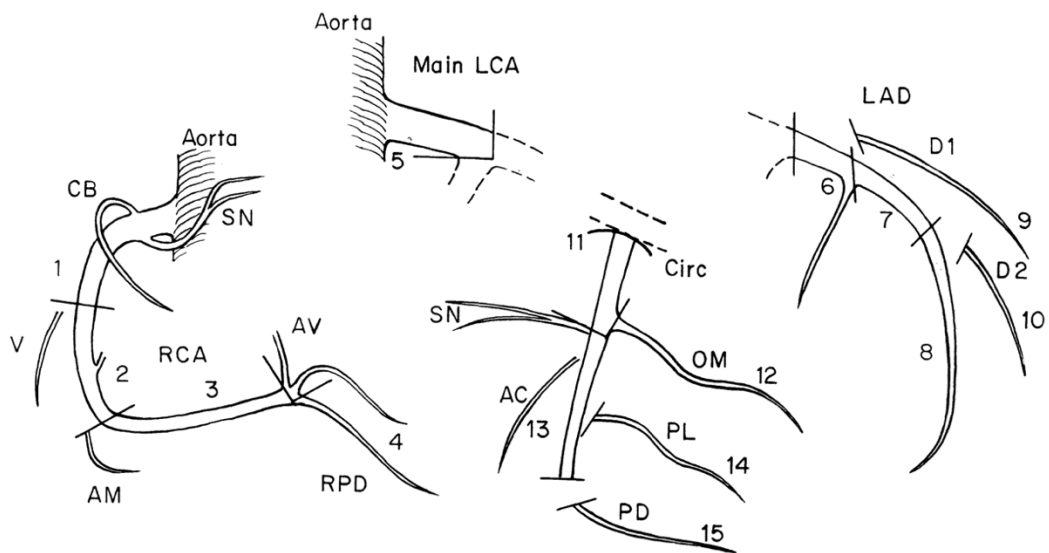


Figure 4. Original schematic representation of coronary arteries anatomy by the American Heart Association¹⁷. 1) Proximal RCA; 2) Mid RCA; 3) Distal RCA; 4) Right posterior descending artery; 5) Left main coronary artery; 6) Proximal LAD; 7) Mid LAD; 8) Distal LAD; 9-10) Diagonal branches of LAD; 11) Proximal LCx; 12) Obtuse marginal branch; 13) Distal LCx; 14) Left posterolateral branch; 15) Posterior descending artery.

4. DUAL-ENERGY IMAGING AND CORONARY CTA

In the last decade, dual-energy imaging has been extended to the study of the cardiovascular system, and in particular of heart and coronary arteries.

However, the use of this technique in clinical practice and its incorporation into guidelines remains limited to research field. This can be attributed to the low availability of dual-energy systems in comparison to conventional scanners, but also to the lack of extensive clinical studies necessary for the definitive validation of the technique.

Nevertheless, initial studies have shown that the use of dual-energy imaging can improve many aspects of CCTA, such as the image quality, the luminal enhancement of the coronary arteries, the radiation dose, and other aspects as well.

4.1. Image quality assessment

Image quality is a result of several factors: it depends on the anthropometric characteristics of the patient and of the imaging system, the scan parameters selected by the operator during image acquisition and the algorithm of reconstruction.

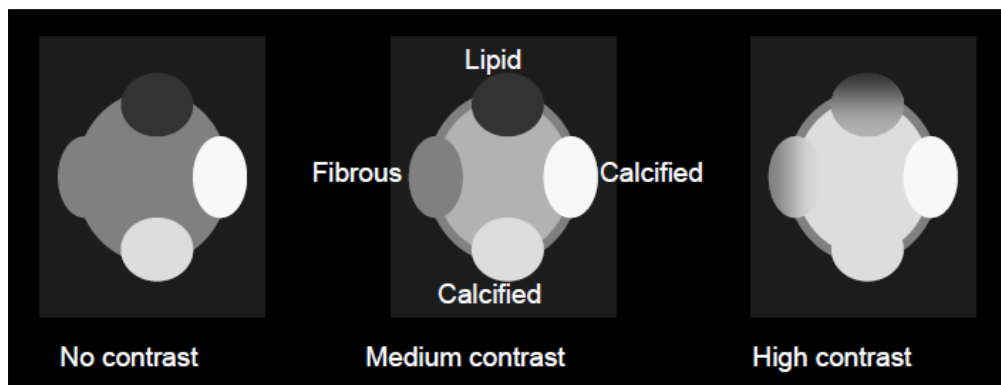


Figure 5. The distinction between the lumen of a vessel and its wall depends on the contrast, therefore on the signal differences between the blood (with or without contrast media), the wall and any other elements present inside the wall.

In the visualization of an organ or a tissue, we evaluate the relationship between the appearance of a single object and its immediate background, rather than the overall characteristics of the image. In computed tomography, tissues and organs are translated into shades of gray: if the contrast between the gray level of each element is sufficient, it's possible to distinguish the displayed elements (Figure).

4.1.1. Objective image quality parameters

In order to define **objective parameters** to assess image quality, contrast is one of the most fundamental characteristics that must be taken into account. However, another key role in image quality is that of noise.

In computed tomography, image **noise** is characterized by an unwanted variation in voxel values in an otherwise homogeneous area: the result is a grainy or textured appearance. It can be measured as the amount of dispersion from the mean value of attenuation of a homogeneous tissue. For example, the standard deviation of the HU value of the subcutaneous fat can be used to assess image noise.

In medical imaging the mean attenuation value and standard deviation of an area of the image can be obtained by placing regions of interest (ROIs) over that area.

Starting from these values, it's possible to compare signal and noise and to derive two of the most used parameters in the objective evaluation of image quality: **signal-to-noise ratio** (SNR) and **contrast-to-noise ratio** (CNR).

SNR can be calculated by relating the mean signal of a region of interest to the background noise. For example, it can be measured by comparing the mean attenuation of the contrast-enhanced blood inside a vessel and the standard deviation of the

subcutaneous fat. However, SNR doesn't consider the contrast between the desired object and the tissue around that object.

For this reason, **CNR** can be calculated by subtracting the signal of the tissue of interest and the signal of the surrounding tissue. The difference in signal is then divided by the noise, resulting in a contrast-to-noise ratio. For example, in the case of the coronary arteries CNR is calculated as the difference between the signal of the contrast-enhanced blood inside the vessels and the signal of the myocardium around the vessel, divided by the background noise of the subcutaneous fat.

4.1.2. Subjective image assessment

The subjective assessment by observers integrates physical measurements into the overall image quality analysis.

It's possible to perform a relative or absolute assessment: the former consists in giving a score to an image by comparing it with a reference standard or with previous images, the latter in assigning an absolute score without any comparison.

One of the most widely used approach to perform an absolute assessment of image quality is by using a **Likert scale** which measures the level of agreement or disagreement for specific statements. Any range of integers can be adopted, but usually a 5-point scale is used. For example, in case of medical imaging, it's possible to assess the level of agreement/disagreement on statements such as "the image has a good sharpness/low noise/low blur". Subsequently, the observers can assign a subjective score, from 1 (completely disagree) to 5 (completely agree), to each statement.

It must be considered that the perceived quality of the image is affected by the display specifications and by parameters such as the display contrast and brightness. In addition,

image viewing conditions such as the lighting and colors of the environment and the distance between the image and the observer may also affect the perceived quality.

For these reasons it's important to maintain standardized conditions during the subjective assessment by different observers.

4.2. Improving image quality

Several studies have described the advantages of DECT for improving signal-to-noise ratio and contrast-to-noise ratio in CCTA. Scheske et al. found that monoenergetic images at 60–80 keV, obtained from a kVps-DECT, could improve signal- and contrast-to-noise ratios in the coronary arteries and myocardium¹⁸.

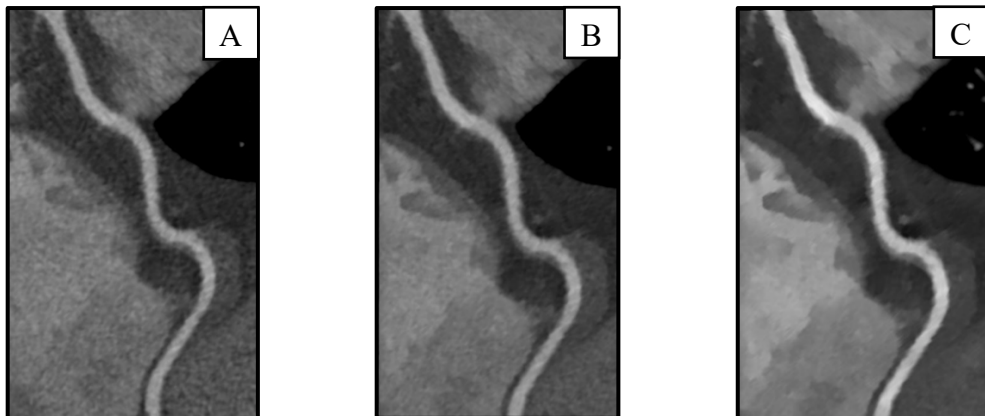


Figure 6. MPR of a coronary artery with at different energy levels. Monoenergetic images at 70 keV (B) and 40 keV (C) shows less noise and a better vascular contrast, especially in 40-keV images, in comparison with conventional images (A).

CNR and SNR of monoenergetic reconstructions at lower energy levels (40-60 keV) can be compromised by the increase in noise that is normally observed at these levels. To overcome the issue, some vendors developed reconstruction algorithms which can reduce image noise in low-energy images. Arendt et al. showed that the use of 40-keV noise-

optimised virtual monoenergetic images allows to significantly improve noise, CNR, SNR and subjective image assessment.¹⁹

Monoenergetic imaging can also be used to decrease blooming artifacts, by reconstructing high-keV images. However, high-energy images show lower vascular contrast in comparison with conventional images and could compromise diagnostic performance (Figure 7).



Figure 7. MPR of dual-layer CT coronary angiography focused on the proximal LAD artery. The image on the left shows a conventional image (A), whereas other images show 75-keV (B) and 120-keV (C) monoenergetic reconstructions. It's possible to observe a progressive improvement in the blooming, especially at 120 keV (C).

4.3. Low-dose contrast media protocols

Many studies have showed that dual-energy imaging allows to reduce the contrast dose, without a deterioration in image quality or diagnostic performance. This can be achieved using low-keV monoenergetic reconstructions, which are closer to the *k-edge* of iodine and allow to increase the attenuation of the contrast media inside the coronary arteries. However, lowering the energy level of the images increases the image noise. Nevertheless, Yan Yi et al. showed that dual-energy spectral detector CT systems suffer less from this phenomenon and can maintain a good image quality even at low energy values with low-dose protocols.²⁰

4.4. Assessing stent patency

Assessing stent restenosis can be challenging due to blooming artifacts caused by the metallic composition. Dual-energy imaging allows for a reduction of these artifacts with high-energy monoenergetic image. Moreover, some vendors offer reconstruction methods which selectively remove iodine from the image. This may help assessing whether the stent is patent or not. However, the use of these techniques for improving stent imaging must be considered experimental, and clinical study are needed to validate their efficacy.

4.5. Virtual non-contrast images for coronary calcium scan

Yamak et al. performed a feasibility study²¹, showing that VNC can be used as a method to quantify the coronary calcium without the necessity of obtaining a pre-contrast acquisition. Similar results were obtained for the aortic valve calcium scoring obtained from VNC in pre-TAVI scans²², although this resulted in an increase in the radiation dose in comparison with conventional protocol.

5. IMPROVED CORONARY ARTERY CONTRAST ENHANCEMENT USING NOISE-OPTIMISED VIRTUAL MONOENERGETIC IMAGING FROM DUAL-SOURCE DUAL-ENERGY CT

Christophe T. Arendt, Rouben Czwikla, Lukas Lenga, Julian L. Wichmann, Moritz H. Albrecht, Christian Booz, Simon S. Martin, Doris Leithner, Patricia Tischendorf, Alfredo Blandino, Thomas J. Vogl, Tommaso D'Angelo

European Journal of Radiology 122(2020):108666 - 10.1016/j.ejrad.2019.108666

5.1. Background

Coronary artery disease (CAD) remains the leading cause of death and morbidity worldwide for both men and women. The diagnostic workup of CAD is increasingly accomplished with coronary computed tomography angiography (CCTA) in symptomatic patients with low to intermediate risk profile²³. Single-energy CCTA is today a robust technique to evaluate the extent of coronary stenoses, showing at the same time very high negative predictive value to exclude obstructive CAD. Current generation computed tomography systems with dual-energy (DECT) capabilities also demonstrate high accuracy to diagnose coronary artery stenosis, and allow for additional first-pass perfusion of the myocardium to investigate ischemia simultaneously²⁴.

Dual-source CT (DSCT) is one of the main system concepts for DECT, using two x-ray tubes and two detectors. Both tubes operate at different voltages to provide material differentiation, which enable to characterize more accurately the various types of atherosclerotic coronary plaques³. Linear blending is commonly used for the standard reconstruction of the DSCT datasets; however, voltage settings are fixed and thus do not

allow to separately alter image impressions at different hypothetical energy levels²⁵. Post-processing of dataset information at various kiloelectron volt (keV) settings can be achieved by virtual monoenergetic imaging (VMI). While this technique may be impaired by increased image noise at low energy levels, noise-optimized algorithms (VMI+) have been recently developed to provide an optimal contrast enhancement at simultaneously lower noise at 40 keV²⁶ according to an energy level towards the k-edge of iodinated contrast media².

Several prior studies have been performed on DSCT platforms to demonstrate improved vascular contrast in different body regions using VMI or VMI+ algorithms^{2,27-29}. As a consequence, higher detection rates for various vascular pathologies, such as stenosis³⁰, bleeding³¹, embolism³² or endoleak³³, have demonstrated the value of such post-processing. However, experience with VMI and VMI+ regarding dual-energy CCTA (DE-CCTA) remains limited and has been mainly focused on the reduction of high-attenuation³⁴ and blooming artifacts³⁵, and on the impact of different coronary plaque components³⁶.

Thus, the aim of our study was to conduct a comprehensive analysis of objective and subjective image quality of VMI and VMI+ reconstructions with regard to the contrast enhancement of coronary arteries and the delineation of coronary plaques in comparison to standard-linearly blended images on a dual-energy DSCT platform.

5.2. Methods

5.2.1. Patient selection

The institutional review board approved the research protocol of this retrospective study with a waiver for written informed patient consent. All procedures were conducted in accordance with the Declaration of Helsinki.

The picture archiving and communication system (PACS) of our clinical centre was searched for patients who underwent a DE-CCTA examination between January 2016 and February 2019. Patients undergoing examinations in single-energy mode were not included. Scans with deviation of the standard contrast media injection protocol (n=12), and with severe respiratory (n=2) or coronary artery motion artifacts (n=7) were excluded. Images with unacceptable quality were defined as comprising at least one coronary artery segment that experienced motion artifacts to an extent that clinical interpretation was not entirely possible. There was no selection of patients based on the body habitus to better represent the clinical scenario. The final study group included 51 patients. All patients were referred because of suspected obstructive CAD. The implementation of these examinations in dual-energy instead of single-energy mode had been performed due to respective research studies or temporary changes in the standard protocols.

5.2.2. DECT image acquisition

All images were acquired on a third-generation dual-source DECT scanner (SOMATOM Force, Siemens Healthcare, Forchheim, Germany). Each patient received one to two sprays of sublingual nitroglycerin (Nitrolingual Spray, G. Pohl-Boskamp GmbH & Co. KG, Hohenlockstedt, Germany). Unless contraindications were present, patients with a heart rate above 60 bpm were administered an injection of 5–10 ml beta-blocker (Metoprolol tartrate, Carinopharm GmbH, Elze, Germany) through an 18-gauge venous cannula in the right elbow pit.

Each patient underwent a prospective ECG-triggered sequential DE-CCTA scan protocol with inspiration breath-hold technique. The scan range of the heart was set on an anteroposterior scout image with the patient in a supine position on the CT table. The contrast agent (CA) (iomeprol, Iomeron 400, Bracco Imaging, Milan, Italy) was administered at a flow rate of 4–5 ml/s following a triphasic protocol (20 ml pure CA; 60 ml mixed bolus with 70% CA and 30% saline; 50 ml pure saline). The optimal individual scan delay time was previously determined by the test-bolus technique (12 ml pure CA; 30 ml saline; flow rate, 4–5 ml/s), using a low-dose dynamic scan at the level of the proximal ascending aorta.

Settings for the DECT mode were as follows: tube A 90 kVp, quality reference current-time product 165 mAs per rotation; tube B 150 kVp with a tin (Sn) filter, 127 mAs per rotation. Pitch was set to 0.15, rotation time to 0.25 s and the collimation was 2×192×0.75 mm. Automated tube current modulation (CARE Dose 4D) was activated in all examinations to optimize individualized radiation dose.

5.2.3. DECT image reconstruction

The raw data was processed using a soft tissue and medium sharp kernel (B40v) and advanced modeled iterative reconstruction (ADMIRE; strength level, 3), with a slice thickness of 0.75mm and an increment of 0.4 mm. Solely best systolic and best diastolic phases of the cardiac cycle, determined by the individual heart rate, were reconstructed.

The default scanner software automatically generated axial linearly-blended images by merging 60% of the low-kV data and 40% of the high-kV data – according to a blending ratio of 0.6 (F_0.6).

For this study, post-processing of the DECT datasets was performed on a 3D multi-modality workstation (syngo.via, version VA30A, Siemens), using both traditional VMI and noise-optimized VMI+ algorithms. Image series were reconstructed at 40, 50, 60, 70, 80, 90 and 100 keV in standard axial projection. Curved multiplanar reconstructions along the vessels' centerline were not reconstructed for the purpose of this study.

5.2.4. Objective image analysis

For the evaluation of objective image quality, signal- and contrast-to-noise ratios of aortic root, left main stem (LMS), left anterior descending (LAD), left circumflex (LCX) and right coronary artery (RCA) were calculated by a radiologist with two years of CCTA experience, who did not participate in the following subjective image interpretation.

For this purpose, mean signal attenuation values (in Hounsfield units [HU]) were measured by placing region-of-interests (ROI) in the contrast-enhanced lumina of the before mentioned vessels. The ROI area was at least 4 mm². Mean HU values of the basal ventricular septum (50 mm²) were measured for the assessment of the image contrast. Additionally, ROIs were placed in the subcutaneous fat anterior to the pectoral muscle (area > 150 mm²) to determine the background noise, derived from the standard deviation (SD) of the measurement.

All computations were performed twice and averaged to reduce measuring inaccuracies. ROIs were always repeated in the exact same location of each image series to ensure consistency. The following formulas were used: $SNR = HU \text{ artery} / SD \text{ fat}$; $CNR = (HU \text{ artery} - HU \text{ myocardium}) / SD \text{ fat}$.

5.2.5. Subjective image analysis

Three radiologists with two to four years of experience in CCTA independently analyzed all linearly-blended and all objectively best rated VMI and VMI+ images. The datasets were evaluated in random order in the dedicated PACS (GE Centricity PACS, GE Healthcare, Chicago, IL). The readers were blinded to the used reconstruction technique and each one could individually modify the preset window settings (F_0.6: width, 700 HU; level, 100 HU; VMI and VMI+: width, 600 HU; level, 150 HU) and the ambient light intensity. Moreover, the different series were evaluated with a minimal time interval of two weeks to avoid recall bias.

The parameters used to evaluate subjective image quality were as follows: vascular contrast, image sharpness, image noise, and, if present, delineation of coronary plaques. Those qualities were rated using a five-point Likert scale. Inter-rater disagreements were not further resolved.

5.2.6. Statistical analysis

All computations were performed using SPSS Statistics (version 24, IBM Corporation, Armonk, NY). Variables are expressed as medians with first (Q1) and third (Q3) quartiles, absolute frequencies, percentages or proportions. To test normality of data distribution, the Kolmogorov-Smirnov test was used. Normal distributed data was analyzed using the analysis of variance (ANOVA) test, non-normal data was computed using the Wilcoxon matched-pairs test. The agreement among all observers was assessed by calculating the intraclass correlation coefficient (ICC) in a two-way mixed model. Levels of agreement were as follows: slight, $ICC \leq 0.20$; fair, $ICC = 0.21-0.40$; moderate, $ICC = 0.41-0.60$; substantial, $ICC = 0.61-0.80$; (almost) perfect, $ICC = 0.81-1.00$ (Landis & Koch). 95% confidence intervals (CI) were reported for each result, if applicable. Values of $p < 0.05$ were considered statistically significant.

5.3. Results

5.3.1. Study population

The study population consisted of 51 patients (median age, 64.0 [Q1: 54.3, Q3: 76.8] years; range, 43–94 years) with a male-female ratio of 2:1. The median value of patient body mass index was 24.5 [22.7, 27.5] kg/m² (range, 17.1–35.6 kg/m²). DE-CCTA showed at least one calcified coronary plaque in 37/51 patients (72.6%).

Prevalence of significant coronary stenosis (> 50% luminal narrowing) on CCTA was 31.4% (16/51). Two representative cases are shown in Figure 8 and 9.

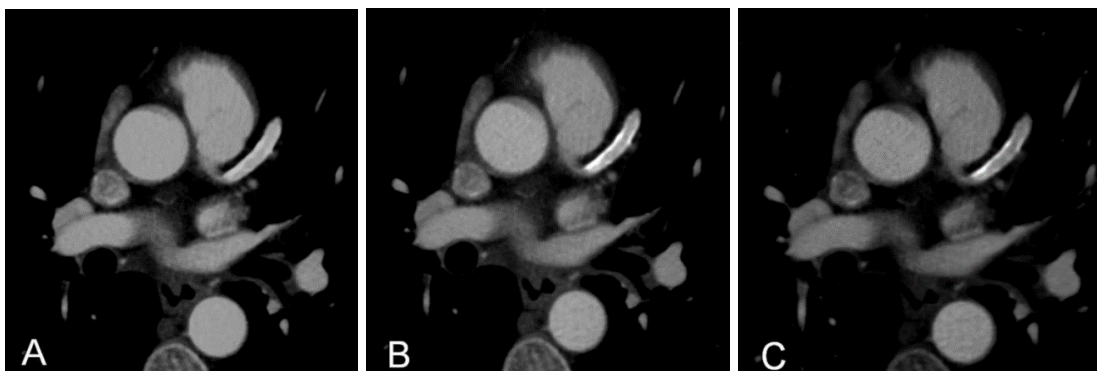


Figure 82. *Clinical Case - 47-year-old male patient with a mild stenosis of the proximal LAD by an eccentric calcified plaque on DE-CCTA. The automatically reconstructed standard linearly-blended images (A) were rated with lower objective and subjective image quality scores in comparison to the VMI/VMI+ series. Images post-processed with 70-keV VMI (B) and particularly the 40-keV VMI+ (C) algorithm revealed superior quality parameters because CNR and SNR were higher and the contrast between the atherosclerotic plaque and the vessel lumen was more pronounced.*

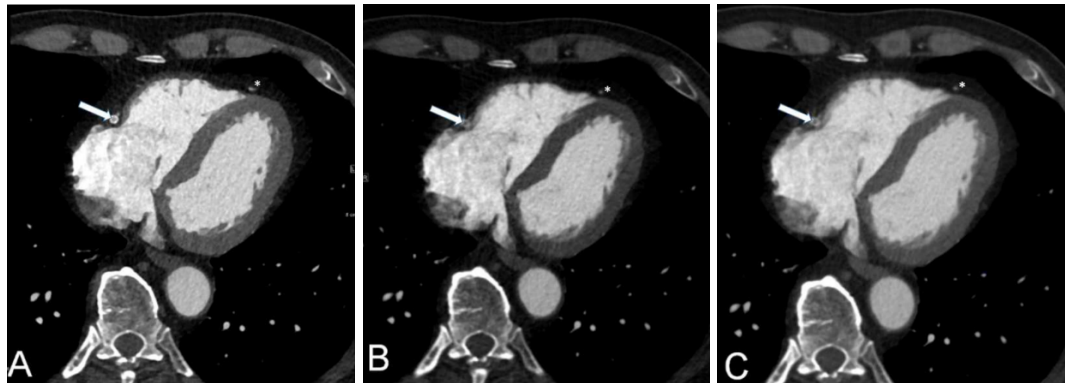


Figure 9. 52-year-old male patient with a stent in the RCA and with clinically suspected stent thrombosis. Standard linearly-blended images (A, arrow) depict clearly the stent, however artificially its size seems to be exaggerated and beam-hardening brightens the lumen. 70-keV VMI (B, arrow) and 40-keV VMI+ (C, arrow) post-processed images substantiate the clinical suspicion due to reduction of artifacts and better image quality. Moreover, the lumen of the LAD appears more distorted in the F_0.6 image (A, asterisk), and the difference of intraluminal contrast between the thrombosed stent and the LAD without stenosis is more pronounced in VMI/VMI+ reconstructions (B/C, asterisk). The stent thrombosis was subsequently confirmed by invasive coronary angiography.

5.3.2. Objective image analysis

The median attenuation of the contrast-enhanced main coronary arteries and aortic root was highest at 40 keV in the VMI+ image series (984.3 [755.0, 1122.2] HU) and at 70 keV in the VMI reconstructions (330.6 [248.6; 391.3] HU). In linearly-blended F_0.6 images, vascular attenuation was 310.5 [261.5; 377.3] HU. Higher values for image noise were observed both in 70-keV VMI (51.8 [45.2; 75.5] HU) and 40-keV VMI+ image series (21.8 [17.0; 24.1] HU) in comparison to F_0.6 images (12.8 [10.9; 15.8] HU) (both $p < 0.001$). In the noise-optimized VMI+ reconstructions, the values for the background noise decreased constantly from 40 keV towards 100 keV (7.4 [6.8; 9.2] HU), whereas lowest SD values were achieved at 70 keV using the traditional VMI algorithm (9.5 [8.3; 11.3]).

Subsequently, values of SNR and CNR of the contrast-enhanced vessels peaked in 40-keV VMI+ reconstructions (44.5 [35.9; 59.1] HU and 33.5 [25.9; 41.4] HU). The 70-keV VMI image series presented significantly lower ($p < 0.001$) SNR (28.1 [20.6; 36.3] HU) and CNR (18.4 [11.9; 27.0] HU) in comparison to SNR and CNR of F_0.6 were significantly lower (23.2 [17.4, 30.6] HU and 15.6 [12.0; 21.3] HU) compared to both VMI and VMI+ algorithms ($p < 0.001$). All results of SNR and CNR measurements are presented as box plots in Figure 10 and 11.

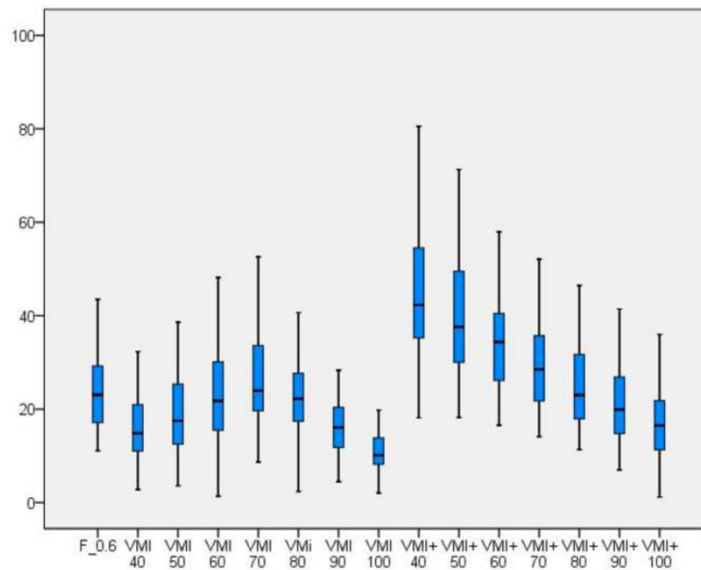


Figure 10. Box plots of data from SNR measurements. Highest SNR values of the coronary arteries and aortic root were calculated for the 40-keV noise-optimized VMI+ reconstructions, significantly superior ($p < 0.001$) to the best results in the traditional VMI series at 70 keV and to the standard linearly-blended images with a blending ratio of 0.6.

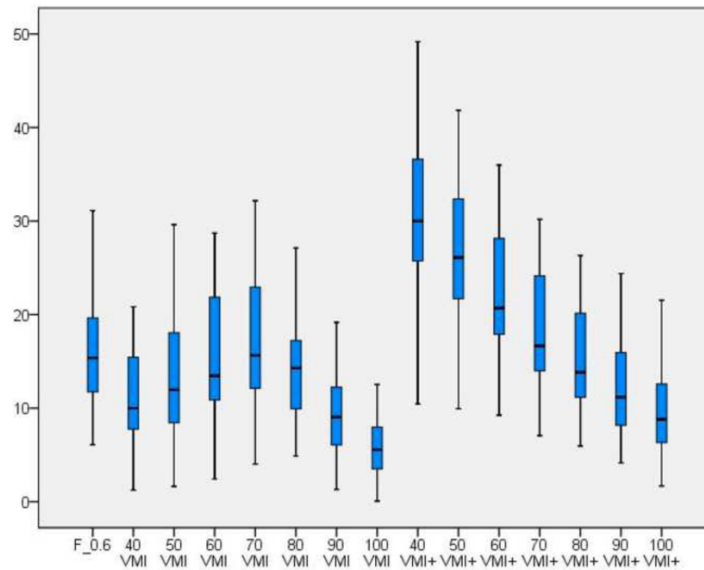


Figure 11. Box plots of data from CNR measurements. Median values for CNR of coronary arteries and aortic root peaked at 40 keV with the noise-optimized VMI+ algorithm and at 70 keV with the traditional algorithm. Results for F_0.6 standard linearly-blended images were lower compared to both VMI techniques. The differences are statistically significant ($p < 0.001$).

5.3.3. Subjective image analysis

Using a five-point Likert scale to rate subjective image parameters, results were best at 40-keV VMI+ series compared to 70-keV VMI and F_0.6 images regarding vascular contrast (median, 5; range, 4–5; $p < 0.001$) and delineation of coronary plaques (median, 5; range, 4–5; $p < 0.001$) with almost perfect inter-rater agreement (ICC, 0.90 and 0.89, respectively). Standard linearly-blended images and images reconstructed with the traditional VMI algorithm at 70 keV both revealed good contrast enhancement of the vessel lumina (median, both 4; range, both 3–5; ICC, 0.85 and 0.88,) and good lesion delineation (median, both 4; ranges, 2–4 and 3–5; ICC, 0.87 and 0.85).

For subjective evaluation of image noise, 40-keV VMI+ and 70-keV VMI series received best rating scores (both median, 4; both range 3–5; ICC, 0.82 and 0.89). Noise in F_0.6 images was considered acceptable (median, 3; range 3–4; ICC, 0.72), but significantly

more pronounced in comparison with the other series ($p < 0.001$). Simultaneously, image sharpness was lowest in the standard linearly blended series (median, 3; range, 2–4) with substantial inter-rater agreement (ICC, 0.69), whereas VMI+ and VMI reconstructions revealed good sharpness of the images (median, both 4; ranges, both 3–5) with almost perfect agreement between raters (ICC, 0.82 and 0.88). Results of median score values and of ICC with 95%CI are summarized in Table 1.

	STANDARD-LINEARLY BLENDED IMAGES	VMI 70 KEV	VMI+ 40 KEV
VASCULAR CONTRAST	4 [3-5] ICC 0.85 [95% CI, 0.77-0.92]	4 [3-5] ICC 0.88 [95% CI, 0.79-0.94]	5 [4-5] ICC 0.90 [95% CI, 0.83-0.94]
LESION DELINEATION	4 [2-4] ICC 0.87 [95% CI, 0.81-0.93]	4 [3-5] ICC 0.85 [95% CI, 0.80-0.92]	5 [4-5] ICC 0.89 [95% CI, 0.80-0.94]
IMAGE NOISE	3 [3-4] ICC 0.72 [95% CI, 0.54-0.83]	4 [3-5] ICC 0.89 [95% CI, 0.81-0.93]	4 [3-5] ICC 0.82 [95% CI, 0.68-0.89]
IMAGE SHARPNESS	3 [2-4] ICC 0.69 [95% CI, 0.45-0.80]	4 [3-5] ICC 0.82 [95% CI, 0.81-0.93]	4 [3-5] ICC 0.88 [95% CI, 0.78-0.94]

Values are expressed as median with ranges in square brackets. CI is given in percentages. CI, confidence interval; ICC, intraclass correlation coefficient; VMI, virtual monoenergetic imaging; VMI+, noise-optimised virtual monoenergetic imaging.

5.4. Discussion

Our hypothesis was that the use of a noise-optimised VMI+ algorithm could be used to improve the contrast of the coronary vasculature during dual-source DE-CCTA. We found that image series reconstructed with the noise-optimised VMI+ algorithm at 40 keV showed best objective and subjective image quality parameters. These images were rated significantly superior to optimal images reconstructed with the traditional algorithm at 70 keV and standard linearly-blended F_{0.6} series, respectively. Optimal delineation of coronary plaques was achieved only with the noise-optimised VMI+ algorithm. In addition, inter-rater agreements for the ratings were almost perfect or substantial.

CCTA in single-energy mode has been established as a robust technique to accurately and non-invasively grade and quantify coronary stenosis. DECT with the use of various post-processing algorithms has been shown to further improve various cardiothoracic applications²⁵. To overcome unfavorable image noise at lower keV using traditional VMI algorithms, a noise-optimizing algorithm was developed, which was predominantly investigated for CT angiography other than cardiac in previous research³⁷. The reconstructions are frequency split and enable, therefore, a separation of the data set into energy bins with lower and higher spatial frequency data sets. Both data sets are combined at the optimal keV level subsequently to achieve an optimal image contrast³⁸. Maximizing vascular enhancement may not be only beneficial in routine DE-CCTA, but could also be applied to examinations with decreased enhancement of the vessel lumen (e.g. patients with low cardiac output or with heart arrhythmia). In addition, multiple prior studies also demonstrated that DECT enables CT angiography with a reduced iodine load of the CA or smaller CA bolus³⁹⁻⁴¹. Thus, CA administration protocols optimized for DECT have also been proposed⁴².

Post-processing of DE-CCTA angiography datasets using VMI/VMI+ algorithms has been evaluated by several prior studies as optimal display of the coronary arteries requires maximization of vascular contrast and minimization of artifacts²⁵. Martin et al. reported substantially improved cardiac contrast in patients undergoing pre-TAVR imaging using DECT⁴³. Symons et al. recently showed that DE-CCTA with low energy levels can improve the CNR of coronary plaque components but also observed that affected volumetric quantification³⁶.

As shown in prior studies evaluating VMI+ in the extracoronary vasculature, the lowest energy level of 40 keV can be expected to reliably provide the highest CNR⁴⁴. However,

it should be emphasized that dedicated windowing settings have to be adapted to make use of the maximized vascular contrast as recently described by D'Angelo et al.⁴⁵.

An additional benefit of the VMI/VMI+ reconstruction techniques in DE-CCTA besides increased CNR is the ability to also drastically reduce artifacts arising from calcified plaque and stents. Mangold et al. performed initial phantom studies and reported optimal artifact reduction at 130 keV in dual-source DECT⁴⁶. Hickethier et al. confirmed these observations also for dual-layer DECT⁴⁷. High-keV VMI/VMI+ reconstructions are also able to reduce blooming artifacts from calcified coronary plaque⁴⁸. This technique can be further extended to DECT-based advanced calcium subtraction which also results in improved reader confidence⁴⁹. Finally, VMI/VMI+ reconstructions are also able to improve contrast in late enhancement imaging during DE-CCTA⁵⁰, demonstrating the flexibility and usefulness of DECT acquisition in clinical routine.

There are certain limitations of this study which warrant discussion.

First, we performed a single-center study with a retrospective design, and further prospective investigations with larger cohorts may be necessary to validate our findings. Second, the raters undertook the subjective image analysis solely of images with the best objective metrics (i.e. 40 keV for VMI+ and 70 keV VMI) and we used the standard linear blending ratio similar to prior studies³⁰. Third, we did not perform a dedicated diagnostic accuracy study as invasive catheter angiography as a reference standard was only present in a fraction of the cases. However, prior publications have demonstrated an increased diagnostic accuracy for the detection of significant vascular stenosis using VMI+DECT⁴⁴. Finally, the majority of coronary plaques found in our study were calcified. Thus, the potential effect of VMI/VMI+ on lipid-rich plaque was not investigated. However, Symons et al.³⁶ recently published a research article that

highlights the impact of monoenergetic reconstructions on different coronary plaque components.

In conclusion, post-processing of DE-CCTA datasets with a noise optimized VMI+ algorithm at the lowest energy level of 40 keV allows for a significant improvement of both luminal contrast of coronary arteries and delineation of calcified atherosclerotic lesions. VMI+ reconstructions showed superior image quality compared to traditional VMI and standard linearly-blended F_0.6 series. This technique may be particularly useful to increase vascular contrast in examinations with reduced iodine load or suboptimal contrast.

6. IMPROVED CORONARY ARTERY CONTRAST ENHANCEMENT USING VIRTUAL MONOENERGETIC IMAGING FROM DUAL-LAYER SPECTRAL DETECTOR CT

Tommaso D'Angelo et al. (submitted)

6.1. Background

Coronary computed tomography angiography (CCTA) has become the preferred non-invasive test for the diagnostic workup of patients with low-moderate risk of coronary artery disease (CAD).

Thanks to its high sensitivity to detect and characterize coronary plaques, its increasingly wide availability, and the speed and ease of execution, CCTA has become a widespread technique in radiologists' clinical activity.

During the last two decades, CCTA diagnostic value has been further expanded by the use of dual-energy computed tomography (DECT) applications.

Dual-energy CCTA (DE-CCTA) has proved to provide information that is unobtainable with conventional single-energy computed tomography. One of the main features of DECT is the post-processing of monoenergetic images at various kilo-electron volt (keV) levels. The technique has shown advantages for both non-contrast and contrast-enhanced DE-CCTA. For example, previous studies have demonstrated that higher monoenergetic levels with cardiac DECT can reduce high-attenuation and blooming artifacts, whereas lower-keV monoenergetic images allow for an improvement of the luminal contrast of coronary arteries and the demarcation of calcified stenosis.

Most of the studies present in scientific literature have been performed on dual-source or rapid-kV switching DECT systems. The recent advent of dual-layer spectral detector CT (DLCT) systems enables simultaneous acquisition of low- and high-kV data from a single detector.

Our hypothesis is that CCTA monoenergetic reconstructions obtained from DLCT platform improves objective and subjective image quality compared to 120 kVp conventional images, without affecting the assessment of coronary stenosis and CCTA diagnostic performance.

6.2. Methods

6.2.1. Study population

Patients' informed consent was waived due to the retrospective and observational nature of the study.

We identified 56 consecutive eligible patients who underwent CCTA on DLCT platform between June 2021 and March 2022 using our internal PACS. Exclusion criteria included (Figure 123): BMI ≤ 18.5 or ≥ 35 (n = 4); severe motion artifacts (n = 4); deviations from the DE-CCTA acquisition protocol due to altered tube voltage settings, kernel settings or contrast media protocol (n = 5); absence of Spectral Base Image (SBI) data (n = 3).

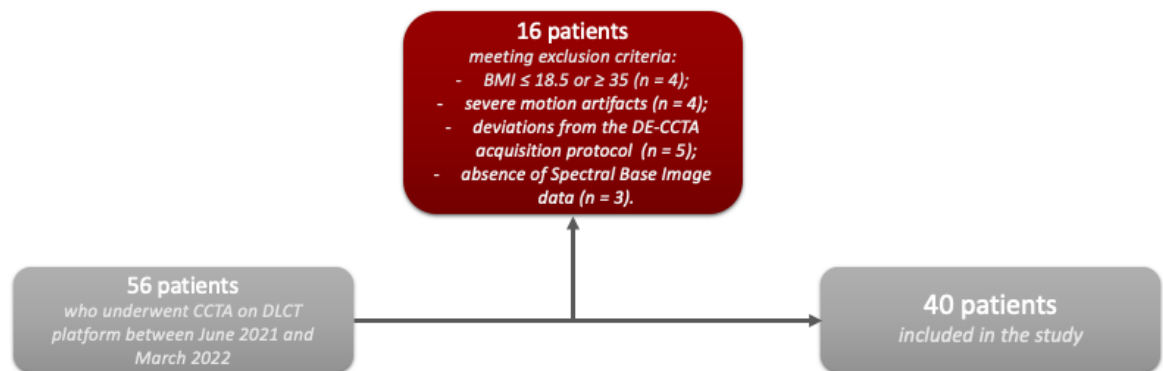


Figure 123. Flowchart showing how patients were included in the study.

Our final patient population consisted of 40 patients (24 males).

6.2.2. DECT acquisition protocol

Examinations were performed using a dual-layer spectral detector CT (DLCT) scanner (IQon Spectral CT, Philips Healthcare, Best, The Netherlands).

Calcium Score CT acquisitions were made using a prospectively ECG-gated protocol at 120 kVp tube voltage and 30 mAs. Images were reconstructed with 3 mm slice thickness and 3 mm increment. Agatston scores were calculated using the vendor software (HeartBeat CS, IntelliSpace Portal, Philips Healthcare).

DE-CCTA scans were performed under deep inspiration breath hold, after the administration of a non-ionic contrast agent (Iomeron 400 mgI/ml; Bracco Imaging SpA, Milan, Italy) at 0.9 mL/kg bodyweight and a flow rate of 5 mL/s. Contrast injection was followed by 50 mL saline chaser. We used automated bolus tracking with a region of interest (ROI) in the ascending aorta at the level of the pulmonary artery with a 160 HU threshold level and a 6 s delay.

Parameters were set as follows: tube voltage = 120 kVp; pitch = 1; FOV = 220 mm; reconstructions were made with a slice thickness of 0.67 mm with an increment of 0.34

mm and a 512x512 matrix. The reconstruction phase corresponded to the 78% of the R-R interval, therefore during diastole. A β -receptor blocker was administered to all patients with a heart rate (HR) ≥ 70 (Esmolol hydrochloride injection, Baxter, Deerfield, Illinois). Before CT scan, all patients received a premedication with a sublingual vasodilator agent (isosorbide dinitrate).

6.2.3. Image reconstruction

Vendor-recommended spectral reconstruction software (Spectral Recon, Philips Healthcare) was used to obtain spectral based images (SBI).

Spectral datasets were reconstructed at six different monoenergetic levels, from 40 to 100 keV, with 10 keV intervals. Conventional datasets were reconstructed using iterative model reconstruction (IMR Cardiac, Philips Healthcare) algorithm.

6.2.4. Objective image quality analysis

All datasets were evaluated with the vendor- software (IntelliSpace Portal Version 8.0, Philips Healthcare) in a dedicated CT workstation.

Each dataset was initially evaluated by a radiologist with more than five years of experience in CCTA. ROIs were placed centrally in the aortic root, in the left main coronary artery, in the proximal segments of the left anterior descending, the circumflex and the right coronary artery, in the basal region of the interventricular septum and in the subcutaneous fat. The ROIs size was not smaller than 2mm².

Measures of the attenuation values (HU) and standard deviations (SD) were repeated twice, averaged, and compared for conventional and monoenergetic images.

For each dataset, we used the following equation to calculate CNR values of coronary vessels⁵¹:

$$(HU_{vessel} - HU_{myocardium})/SD_{fat}$$

SNR was calculated as follows:

$$SNR = HU_{vessel}/SD_{fat}$$

6.2.5. Subjective image assessment

Axial images, multi-planar and volume rendering reconstructions of conventional and monoenergetic images at 40 keV and 70 keV were used for the analysis.

Two radiologists with five and ten years of experience in cardiovascular imaging independently assessed image quality of each dataset using a 5-point Likert scoring system (1: poor quality, not diagnostic; 2: sufficient; 3: satisfactory; 4: good; and 5: excellent). Readers were blinded to the type of dataset and they evaluated each of the following parameters: Sharpness; Vascular Contrast; Image Noise; Stenosis Demarcation; Overall impression.

All datasets were evaluated using an initial window width/level of 900/100 HU, as recommended by the vendor, however, window settings could be subjectively adjusted by the readers.

Scores were averaged and compared for conventional and monoenergetic datasets.

6.2.6. Coronary stenosis assessment

All CCTA datasets (i.e. *conventional*, *VMI 40 keV* and *VMI 70 keV*) were reformatted using true axial and curved multiplanar reconstructions, and the degree of stenosis was semiautomatically assessed by the vendor software (Stenosis analysis, Intellispace Portal).

The degree of stenosis was expressed in percentage and the values were categorized as suggested by the SCCT grading for stenosis, in the following six groups: 0%, 1%-24%, 25%-49%, 50%-69, 70-99% and 100%,⁵²

6.2.7. Statistical analysis

Statistical analysis was performed using SPSS Statistics software (version 26.0, IBM). The Shapiro–Wilk test was used to assess normality of data distribution.

Continuous variables were described as mean \pm SD if normally distributed, or median (IQR) for non-normally distributed data.

To test differences between variables, analysis of variance (ANOVA) test was used for normally distributed data, while non-normal data was analyzed using the Wilcoxon matched-pairs signed rank test. A p-value < 0.05 was used to confirm a statistically significant difference.

For subjective image quality, inter-observer agreement was calculated with the Cohen-kappa statistic (k). The Cohen-kappa statistic was also used to evaluate the correlation among conventional dataset and monoenergetic reconstructions for grading of stenoses.

Results were interpreted as follows: slight or poor agreement ($k < 0.20$), fair agreement ($k = 0.20–0.40$), moderate agreement ($k = 0.40–0.60$), good agreement ($k = 0.60–0.80$), and excellent agreement ($k > 0.80$).

To further assess coronary stenosis agreement, the Bland-Altman method was used to evaluate bias between mean differences and limits of agreement (LOA) in a head-to-head comparison between conventional and 70-keV images and conventional and 40-keV images.

6.3. Results

6.3.1. Study population

Image datasets from a total of 40 patients (mean age of 60.7 ± 11.8 years) were analyzed. The mean body mass index was 25.8 ± 3.8 . The mean Agatston calcium score was 234.3 ± 232.6 , with the presence of at least one calcified coronary plaque in 19/40 patients. The patients' demographic characteristics are summarized in Table 1.

Characteristics	Both sexes	Men	Women
Number (%)	40 (100%)	24 (60.0%)	16 (40.0%)
Age (years): Mean (SD)	60.73 (11.8)	61.2 (12.2)	60.0 (11.6)
BMI: Mean (SD)	25.8 (3.8)	26.4 (4.2)	24.9 (3.1)
<ul style="list-style-type: none"> • 18.5-24.9: number (%) • 25-29.9: number (%) • 30-34.9: number (%) 	<ul style="list-style-type: none"> • 21 (52.5%) • 14 (35%) • 5 (12.5%) 	<ul style="list-style-type: none"> • 12 (50.0%) • 8 (33.3%) • 4 (16.7%) 	<ul style="list-style-type: none"> • 9 (56.3%) • 6 (37.5%) • 1 (6.2%)
Calcium Score (Agatston): Mean (SD)	234.3 (232.6)	274.9 (243.7)	177.5 (211.0)
CAC-DRS:			
<ul style="list-style-type: none"> • A: median (IQR) • N: median (IQR) 	<ul style="list-style-type: none"> 2 (0-3) 1 (0-3) 	<ul style="list-style-type: none"> 3 (0-3) 1.5 (0-3) 	<ul style="list-style-type: none"> 1 (0-3) 0.5 (0-1.5)

Table 1. Demographic characteristics of study population.

6.3.2. Objective image quality analysis

Objective image quality analysis was performed by measurement of mean attenuation, noise, SNR, and CNR for each coronary vessel.

As for mean attenuations, distribution of the values was normal for each vessel. Attenuation progressively increased for monoenergetic reconstructions with lower KeV, as normally expected. The mean attenuation of coronary arteries in conventional images ($464.94 \text{ HU} \pm 66.39 \text{ HU}$) was significant lower in comparison with 70-keV monoenergetic images ($515,20 \text{ HU} \pm 82.85 \text{ HU}$, $p = 0.03$), according to literature data.

70keV VMI images showed lower noise ($8.66 \text{ HU} \pm 1.84 \text{ HU}$) than conventional images ($11.58 \text{ HU} \pm 2.84 \text{ HU}$, $p < 0.001$) and 40keV monoenergetic images ($10.96 \text{ HU} \pm 2.91 \text{ HU}$, $p < 0.001$). The mean image noise of 40-keV monoenergetic reconstructions was lower than conventional images, although not significantly ($p = 0.83$). Overall, the mean values for noise constantly decreased from 40-keV towards 100 keV monoenergetic reconstructions, and the difference with conventional images became statistically significant from 50keV VMI ($9.63 \text{ HU} \pm 2.24 \text{ HU}$, $p = 0.002$).

Subsequently, values of SNR and CNR of the vessels are higher in lower-keV monoenergetic images and progressively decrease towards 100 keV reconstructions. In particular, all reconstructions from 70-keV to 40-keV showed significantly higher SNR (from 61.33 ± 12.46 to 154.22 ± 42.91 , respectively) and CNR (from 51.45 ± 11.19 to 135.63 ± 39.38 , respectively) than conventional images (all $p < 0.001$).

Values of mean attenuation for each vessel and of subcutaneous fat noise are presented in Table 2. The value of the signal- and contrast-to-noise ratio results are presented as box plots in Figure 13.

	Conventional	100 keV	90 keV	80 keV
Aorta				
• Attenuation	443.93 ± 59.05	241.3 ± 33.49	298.18 ± 44.21	381.51 ± 59.37
• SNR	40.49 ± 10.50	29.73 ± 5.72	36.84 ± 7.48	46.78 ± 9.37
• CNR	32.96 ± 9.21	22.94 ± 5.15	29.33 ± 6.67	38.23 ± 8.47
L.main				
• Attenuation	451.28 ± 62.68	251.47 ± 40.21	306.01 ± 48.62	387.60 ± 62.96
• SNR	40.68 ± 10.73	30.89 ± 5.84	37.73 ± 7.42	47.47 ± 9.27
• CNR	33.14 ± 9.51	24.10 ± 5.41	30.22 ± 6.66	38.92 ± 8.35
LAD				
• Attenuation	464.61 ± 76.37	254.02 ± 51.29	307.36 ± 58.85	387.17 ± 72.2
• SNR	42.42 ± 11.75	31.11 ± 6.70	37.76 ± 7.92	47.39 ± 9.84
• CNR	34.88 ± 10.57	24.33 ± 6.56	30.25 ± 7.48	38.84 ± 9.13
LCx				
• Attenuation	474.79 ± 77.09	269.73 ± 45.10	324.66 ± 53.73	404.49 ± 68.73
• SNR	43.08 ± 10.96	32.90 ± 5.04	39.81 ± 6.90	49.33 ± 8.90
• CNR	35.55 ± 9.85	26.11 ± 4.96	32.31 ± 6.32	40.78 ± 8.07
RCA				
• Attenuation	474.57 ± 83.68	251.12 ± 42.64	307.58 ± 52.30	388.67 ± 65.68
• SNR	42.90 ± 10.84	30.62 ± 4.89	37.74 ± 7.31	47.44 ± 9.26
• CNR	35.37 ± 9.87	23.83 ± 4.57	30.23 ± 6.52	38.89 ± 8.25
Noise (SD)	11.53 ± 2.84	8.32 ± 1.47	8.34 ± 1.59	8.39 ± 1.65

	70-keV	60 keV	50 keV	40-keV
Aorta				
• Attenuation	521.14 ± 83.51	717.33 ± 120.84	1064.17 ± 182.13	1673.69 ± 281.09
• SNR	60.94 ± 12.75	82.33 ± 16.86	114.42 ± 25.48	157.42 ± 40.46
• CNR	51.05 ± 11.68	70.27 ± 15.80	99.74 ± 23.98	138.84 ± 37.79
L.main				
• Attenuation	510.30 ± 81.94	717.67 ± 121.15	1044.98 ± 182.33	1605.15 ± 284.26
• SNR	60.89 ± 12.83	81.99 ± 18.03	113.02 ± 27.99	155.18 ± 44.57
• CNR	51.00 ± 11.63	69.93 ± 16.70	98.34 ± 26.07	136.59 ± 41.41
LAD				
• Attenuation	510.47 ± 93.91	704.19 ± 129.29	1031.51 ± 186.08	1578.37 ± 288.46
• SNR	60.79 ± 13.53	81.09 ± 18.69	111.45 ± 27.91	152.58 ± 44.26
• CNR	50.90 ± 12.43	69.03 ± 17.36	96.67 ± 25.91	133.99 ± 40.92
LCx				
• Attenuation	526.31 ± 92.64	720.30 ± 133.11	1044.94 ± 197.95	1591.35 ± 310.15
• SNR	62.55 ± 12.68	82.74 ± 17.96	112.59 ± 27.56	153.43 ± 44.73
• CNR	52.66 ± 11.48	70.68 ± 16.43	97.90 ± 25.42	134.84 ± 41.21
RCA				
• Attenuation	513.7 ± 86.51	714.62 ± 118.83	1049.19 ± 174.94	1613.62 ± 258.94
• SNR	61.11 ± 13.08	82.17 ± 18.16	113.24 ± 27.56	155.71 ± 42.23
• CNR	51.22 ± 11.74	70.11 ± 16.42	98.55 ± 25.27	137.11 ± 39.56
Noise (SD)	8.66 ± 1.84	8.97 ± 1.96	9.63 ± 2.24	10.96 ± 2.91

Table 2. Results presented as mean (HU) ± SD for objective image analysis. Attenuation, signal-to-noise ratio (SNR) and contrast-to-noise ratio (CNR) are reported for ascending aorta, left main coronary artery (L.main), left anterior descending artery (LAD), left circumflex coronary artery (LCx), right coronary artery (RCA). The standard deviation of subcutaneous fat is reported for image noise.

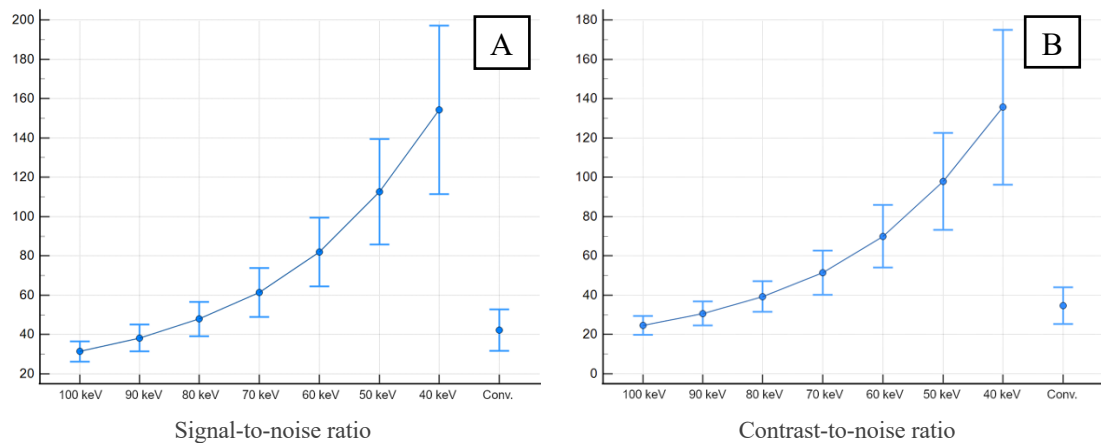


Figure 134. SNR (A) and CNR (A), presented as boxplots, show higher values for 40-keV monoenergetic reconstructions, when compared both with other monoenergetic reconstructions and conventional images.

6.3.3. Subjective image assessment

A five-point Likert scale was used by two experienced radiologists to rate subjective image parameters. The inter-reader agreement was good for all the parameters. Indeed, the kappa values for image noise, sharpness, vascular contrast both for conventional and 70 and 40-keV monoenergetic images were all above 0.60.

40-keV monoenergetic images got the best average score for sharpness, vascular contrast, and for overall impression (all $p < 0.001$). However, 70-keV monoenergetic images got a better score for sharpness, vascular contrast and for overall impression compared with conventional images (all with $p < 0.001$).

70-keV monoenergetic images were rated as the less noisy (all $p < 0.001$). The difference in the noise scores between conventional and 40-keV monoenergetic images was not significant ($p = 0.06$), despite 40 keV VMI obtained higher scores.

Stenosis demarcation got better scores either with 70-keV and 40-keV reconstructions in comparison with conventional images (both $p < 0.001$). The difference between 40-keV and 70-keV isn't significant ($p = 0.096$).

The median of average scores with 95% confidence interval (CI) for each parameter, with the inter-reader agreement are presented in Table 3 and in Figure 14. The p-value that results from the comparison of the average score between each dataset is presented in Table 4.

	Conventional images	70-keV MonoE images	40-keV MonoE images
Image sharpness	3.5 (3-4) $k = 0.67 [0.47 - 0.87]$	4 (3.5-4) $k = 0.64 [0.44 - 0.84]$	4.25 (4-5) $k = 0.70 [0.49 - 0.91]$
Image noise	3 (2.5-3) $k = 0.64 [0.42 - 0.87]$	4 (3-4) $k = 0.66 [0.46 - 0.86]$	4 (3.5-4) $k = 0.64 [0.46 - 0.82]$
Vascular contrast	3.5 (3-4) $k = 0.68 [0.47 - 0.88]$	4 (4-4) $k = 0.67 [0.47 - 0.88]$	4.5 (4-5) $k = 0.68 [0.49 - 0.89]$
Stenosis demarcation	3 (3-4) $k = 0.81 [0.70 - 0.93]$	3.5 (3-4) $k = 0.76 [0.61 - 0.91]$	4 (3.5-4) $k = 0.73 [0.58 - 0.89]$
Overall impression	3 (3-4) $k = 0.62 [0.41 - 0.84]$	4 (3.5-4) $k = 0.61 [0.36 - 0.86]$	4.75 (4-5) $k = 0.77 [0.57 - 0.97]$

Table 3. Average scores by two readers for each characteristic. Reported as median (IQR); kappa (95 CI).

	Conventional vs 70-keV	Conventional vs 40-keV	70-keV vs 40-keV
Image sharpness	$p < 0.001$	$p < 0.001$	$p < 0.001$
Image noise	$p < 0.001$	$p = 0.061$	$p < 0.001$
Vascular contrast	$p < 0.001$	$p < 0.001$	$p < 0.001$
Stenosis demarcation	$p = 0.018$	$p < 0.001$	$p = 0.096$
Overall impression	$p < 0.001$	$p < 0.001$	$p < 0.001$

Table 4. Statistical significance expressed as p-value for each comparison between conventional and monoenergetic images. 70- and 40-keV monoenergetic reconstructions show better subjective image parameters in comparison with conventional images.

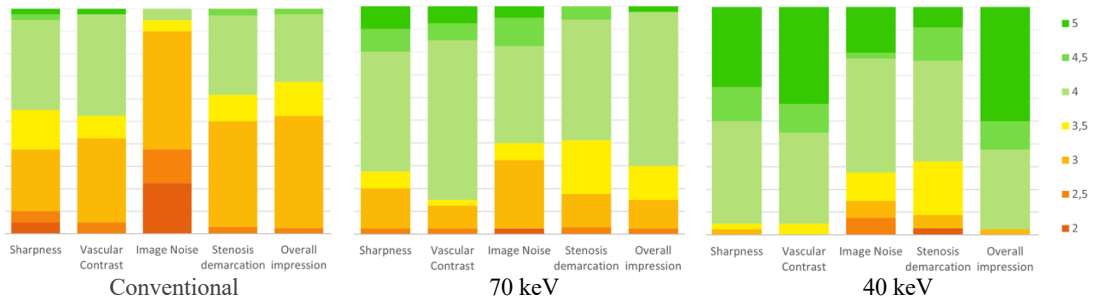


Figure 145. Bar plot shows results of the analysis of subjective image quality. Sharpness, vascular contrast, image noise, usability for stenosis demarcation, and overall image quality were rated by two observers. The values shown are the average of the scores given by the two observers. 70-keV and 40-keV monoenergetic reconstructions show better subjective results if compared to conventional images.

6.3.4. Coronary stenosis assessment

The grading of stenosis of coronary arteries in 5 different categories, as suggested by the SCCT⁵², showed excellent inter-rater agreement (overall $k = 0.94$ [0.91-0.97]) among conventional and monoenergetic images at 70 keV and 40 keV.

The inter-rater agreement was higher if calculated between conventional and 70-keV monoenergetic images ($k = 0.97$ [0.95 – 0.99]), as expected due to the visual similarity between the images. All the results for inter-rater agreement are presented in Table 5. More information regarding different grading at different image reconstructions are described per-vessel in Table 6.

	SCCT grading (Cohen's Kappa)
Conventional vs 70-keV	0.97 [0.95 – 0.99]
Conventional vs 40-keV	0.88 [0.82 – 0.95]
70-keV vs 40-keV	0.93 [0.91 – 0.97]

Table 5. Inter-rater agreement for stenosis in the comparison of conventional and monoenergetic images.

Artery	Conv.	70-keV	40-keV
L. Main			
- 0%	33	33	33
- 1-24%	3	4	4
- 25-49%	3	2	2
- 50-69%	1	1	1
- 70-99%	0	0	0
- 100%	0	0	0
LAD			
- 0%	8	8	8
- 1-24%	11	10	12
- 25-49%	9	10	8
- 50-69%	7	7	6
- 70-99%	5	5	6
- 100%	0	0	0
LCx			
- 0%	18	18	18
- 1-24%	9	8	8
- 25-49%	7	8	8
- 50-69%	2	1	4
- 70-99%	4	5	2
- 100%	0	0	0
RCA			
- 0%	14	14	14
- 1-24%	9	9	10
- 25-49%	12	12	9
- 50-69%	3	3	5
- 70-99%	2	2	2
- 100%	0	0	0

Table 6. Stenosis grading for each vessel with conventional and monoenergetic imaging after semi-automated analysis with vendor-suggested software. *L.Main*: Left main coronary artery; *LAD*: Left anterior descendent coronary artery; *LCx*: left circumflex coronary artery; *RCA*: Right coronary artery

A Bland-Altman plot is presented in Figure 15 to compare the agreement concerning the percentage of stenosis among conventional, 70- and 40-keV monoenergetic images. It showed close agreement and a mean difference of -0.7% in the quantification of stenosis between conventional and 70-keV images [-1.0152 – -0.3641], with narrow LOA (-3.68 to 2.30). The mean difference between conventional and 40-keV images, was even smaller [-0.2% (-0.79 – 0.74)] despite larger LOA (-7.06 to 7.02).

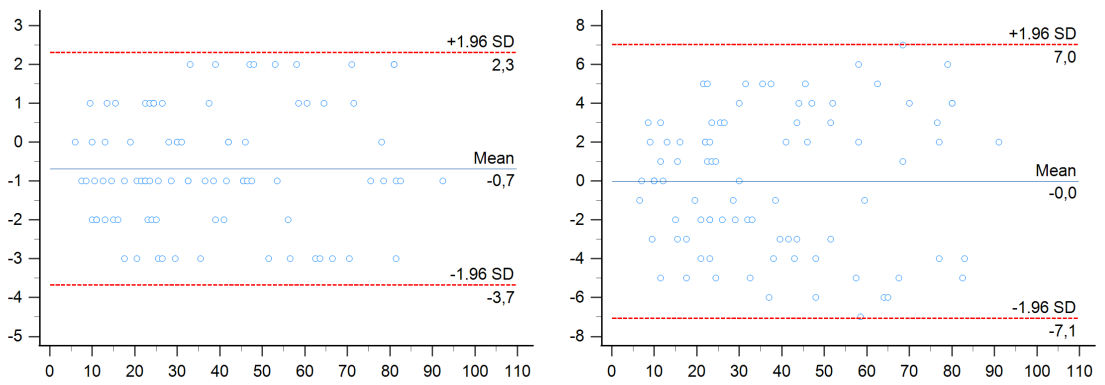


Figure 15. Bland-Altman plot comparing the diagnostic accuracy between conventional images and 70- and 40-keV images.

6.4. Discussion

We compared the objective and subjective image quality of monoenergetic images and conventional images of CCTA exams performed on a dual-layer spectral detector CT platform. We found that lower-keV images showed best objective image quality, with highest values for contrast- and signal-to-noise ratio.

Subjective image quality parameters were also better for 40-keV monoenergetic images, but even 70-keV reconstructions were assigned better scores than conventional images.

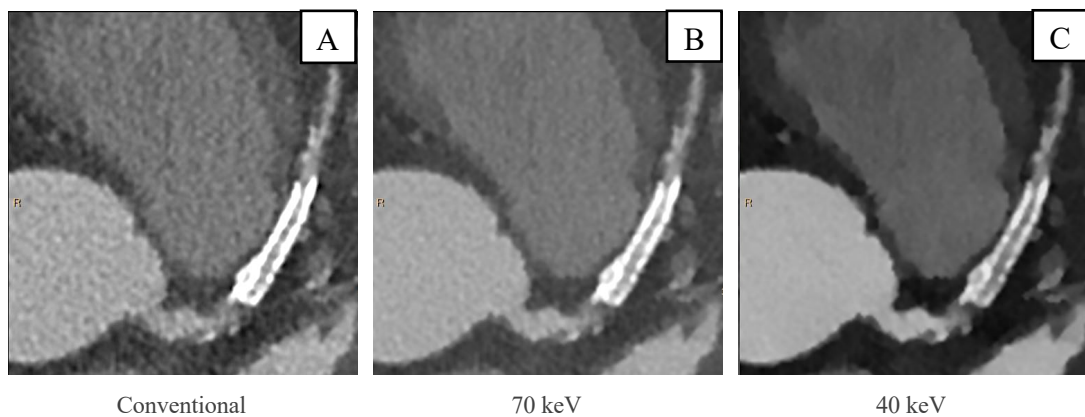


Figure 16. Conventional (A), 70-keV (B) and 40-keV (C) images on the axial plane showing the aortic root at the level of the left coronary ostium. Monoenergetic images (B-C), especially 40-keV reconstructions (C), show a better image sharpness and noise in comparison with conventional images (A). Moreover, 40-keV reconstructions (C) allow to better assess the patency of the metallic stent in the proximal segment of the LAD.

In particular, 40-keV monoenergetic images offered the best results either at objective and subjective analysis (Figure 16). The higher attenuation of iodine at low-keV reconstructions results in highest values for SNR and CNR and determines the best vascular contrast. This is due to the highest attenuation of iodine when the energy level is closer to its k-edge of 33.2 keV²⁹. However, previous studies have shown some limitations in the use of low-keV reconstructions. Firstly, low-keV images are

responsible for an increase of high-attenuation³⁴ and blooming artifacts that may lead to a worse agreement in terms of coronary stenosis grading³⁵. In our study, Bland-Altman analysis showed only a small mean difference between conventional and 40-keV monoenergetic images for the grading of coronary stenosis at semiautomatic quantitative analysis.

Moreover, despite image noise and energy level are inversely associated in VMI, we didn't notice a significant increase of noise compared to conventional images even at low-keV reconstructions. This can be partially explained with the fact that we used a DLCT system that can reduce the image noise at low energy levels due to spectral detector technology²⁰. Low-keV images have allowed to obtain optimal contrast enhancement, even using lower dose of contrast media, and maintaining good image quality⁵⁴.

Different vendors of dual-energy CT platforms, such as rapid kV-switching or dual-source, have developed noise-optimized algorithms to improve image quality of low-keV monoenergetic images³⁰.

Our results showed that 40-keV images showed the best results in terms of SNR and CNR with similar noise levels than conventional images. In addition, 70-keV images did guarantee an improvement in terms of noise compared to conventional and 40-keV images, with higher scores at subjective assessment.

We also observed that the quantification of stenosis showed a good agreement among conventional images and 70-keV and 40-keV monoenergetic reconstructions. However, optimal image quality needed manual adjustment of window settings by the readers to avoid blooming of the vessel, which might be dependent on the experience of the reader.

Moreover, unlike with other dual-energy imaging techniques, DLCT allows for direct visualization of monoenergetic images from spectral data and to switch at different energy levels, without the need of reconstructing each monoenergetic dataset at the moment of exam acquisition.

We can affirm that performing a CCTA on a dual-layer system, can definitively benefit of routine use of monoenergetic imaging. In clinical practice this can translate in better image quality without compromising stenosis quantification. Moreover, the spectral data acquired during CCTA may allow the radiologist to obtain additional information such as perfusion imaging⁵⁵ or to better assess late-iodine enhancement (LIE) on delayed phase⁵⁰. Additionally, higher CNR of low keV images might allow to perform CCTA with lower volumes of contrast media.

Our study has several limitations. Firstly, it is a single center study with a retrospective design. Secondly, we didn't use coronary angiography to assess the grade of coronary stenosis. Thirdly, our sample size is limited and larger studies with prospective design are needed.

REFERENCES

1. Knuuti J, Wijns W, Saraste A, Capodanno D, Barbato E, Funck-Brentano C, Prescott E, Storey RF, Deaton C, Cuisset T, Agewall S, Dickstein K, Edvardsen T, Escaned J, Gersh BJ, Svitil P, Gilard M, Hasdai D, Hatala R, Mahfoud F, Masip J, Muneretto C, Valgimigli M, Achenbach S, Bax JJ; ESC Scientific Document Group. 2019 ESC Guidelines for the diagnosis and management of chronic coronary syndromes. *Eur Heart J*. 2020 Jan 14;41(3):407-477. doi: 10.1093/eurheartj/ehz425. PMID: 31504439.
2. Danad I, Fayad ZA, Willemink MJ, Min JK. New Applications of Cardiac Computed Tomography: Dual-Energy, Spectral, and Molecular CT Imaging. *JACC Cardiovasc Imaging*. 2015 Jun;8(6):710-23. doi: 10.1016/j.jcmg.2015.03.005. PMID: 26068288; PMCID: PMC4467470.
3. Johnson TR, Krauss B, Sedlmair M, Grasruck M, Bruder H, Morhard D, Fink C, Weckbach S, Lenhard M, Schmidt B, Flohr T, Reiser MF, Becker CR. Material differentiation by dual energy CT: initial experience. *Eur Radiol*. 2007 Jun;17(6):1510-7. doi: 10.1007/s00330-006-0517-6. PMID: 17151859.
4. Yu L, Leng S, McCollough CH. Dual-energy CT-based monochromatic imaging. *AJR Am J Roentgenol*. 2012 Nov;199(5 Suppl):S9-S15. doi: 10.2214/AJR.12.9121. PMID: 23097173.
5. Richmond C. Sir Godfrey Hounsfield. *BMJ*. 2004 Sep 18;329(7467):687. PMCID: PMC517662.

6. Brenner DJ, Hall EJ. Computed tomography--an increasing source of radiation exposure. *N Engl J Med.* 2007 Nov 29;357(22):2277-84. doi: 10.1056/NEJMra072149. PMID: 18046031.
7. Bushberg JT. The AAPM/RSNA physics tutorial for residents. X-ray interactions. *Radiographics.* 1998 Mar-Apr;18(2):457-68. doi: 10.1148/radiographics.18.2.9536489. PMID: 9536489.
8. Flohr, T. CT Systems. *Curr Radiol Rep.* 2013; 1:52–63. doi: 10.1007/s40134-012-0005-5
9. Kachelriess M, Ulzheimer S, Kalender WA. ECG-correlated image reconstruction from subsecond multi-slice spiral CT scans of the heart. *Med Phys.* 2000 Aug;27(8):1881-902. doi: 10.1118/1.1286552. PMID: 10984235.
10. Rybicki FJ, Otero HJ, Steigner ML, Vorobiof G, Nallamshetty L, Mitsouras D, Ersoy H, Mather RT, Judy PF, Cai T, Coyner K, Schultz K, Whitmore AG, Di Carli MF. Initial evaluation of coronary images from 320-detector row computed tomography. *Int J Cardiovasc Imaging.* 2008 Jun;24(5):535-46. doi: 10.1007/s10554-008-9308-2. PMID: 18368512.
11. Flohr TG, McCollough CH, Bruder H, Petersilka M, Gruber K, Süß C, Grasruck M, Stierstorfer K, Krauss B, Raupach R, Primak AN, Küttner A, Achenbach S, Becker C, Kopp A, Ohnesorge BM. First performance evaluation of a dual-source CT (DSCT) system. *Eur Radiol.* 2006 Feb;16(2):256-68. doi: 10.1007/s00330-005-2919-2. PMID: 16341833.
12. McCollough CH, Leng S, Yu L, Fletcher JG. Dual- and Multi-Energy CT: Principles, Technical Approaches, and Clinical Applications. *Radiology.* 2015 Sep;276(3):637-53. doi: 10.1148/radiol.2015142631. PMID: 26302388; PMCID: PMC4557396.

13. Manning WJ, Li W, Edelman RR. A preliminary report comparing magnetic resonance coronary angiography with conventional angiography. *N Engl J Med*. 1993 Mar 25;328(12):828-32. doi: 10.1056/NEJM199303253281202. Erratum in: *N Engl J Med* 1993 Jan 13;330(2):152. PMID: 8285929.
14. Achenbach S, Moshage W, Ropers D, Nossen J, Daniel WG. Value of electron-beam computed tomography for the noninvasive detection of high-grade coronary-artery stenoses and occlusions. *N Engl J Med*. 1998 Dec 31;339(27):1964-71. doi: 10.1056/NEJM199812313392702. PMID: 9869667.
15. Miller JM, Rochitte CE, Dewey M, Arbab-Zadeh A, Niinuma H, Gottlieb I, Paul N, Clouse ME, Shapiro EP, Hoe J, Lardo AC, Bush DE, de Roos A, Cox C, Brinker J, Lima JA. Diagnostic performance of coronary angiography by 64-row CT. *N Engl J Med*. 2008 Nov 27;359(22):2324-36. doi: 10.1056/NEJMoa0806576. PMID: 19038879.
16. Gulati M, Levy PD, Mukherjee D, Amsterdam E, Bhatt DL, Birtcher KK, Blankstein R, Boyd J, Bullock-Palmer RP, Conejo T, Diercks DB, Gentile F, Greenwood JP, Hess EP, Hollenberg SM, Jaber WA, Jneid H, Joglar JA, Morrow DA, O'Connor RE, Ross MA, Shaw LJ. 2021 AHA/ACC/ASE/CHEST/SAEM/SCCT/SCMR Guideline for the Evaluation and Diagnosis of Chest Pain: A Report of the American College of Cardiology/American Heart Association Joint Committee on Clinical Practice Guidelines. *Circulation*. 2021 Nov 30;144(22):e368-e454. doi: 10.1161/CIR.0000000000001029. PMID: 34709879.
17. Austen WG, Edwards JE, Frye RL, Gensini GG, Gott VL, Griffith LS, McGoon DC, Murphy ML, Roe BB. A reporting system on patients evaluated for coronary artery disease. Report of the Ad Hoc Committee for Grading of Coronary Artery

- Disease, Council on Cardiovascular Surgery, American Heart Association. *Circulation*. 1975 Apr;51(4 Suppl):5-40. doi: 10.1161/01.cir.51.4.5. PMID: 1116248.
18. Scheske JA, O'Brien JM, Earls JP, Min JK, LaBounty TM, Cury RC, Lee TY, So A, Hague CJ, Al-Hassan D, Kuriyabashi S, Dowe DA, Leipsic JA. Coronary artery imaging with single-source rapid kilovolt peak-switching dual-energy CT. *Radiology*. 2013 Sep;268(3):702-9. doi: 10.1148/radiol.13121901. PMID: 23579045.
 19. Arendt CT, Czwikla R, Lenga L, Wichmann JL, Albrecht MH, Booz C, Martin SS, Leithner D, Tischendorf P, Blandino A, Vogl TJ, D'Angelo T. Improved coronary artery contrast enhancement using noise-optimised virtual monoenergetic imaging from dual-source dual-energy computed tomography. *Eur J Radiol*. 2020 Jan;122:108666. doi: 10.1016/j.ejrad.2019.108666. PMID: 31786506.
 20. Yi Y, Zhao XM, Wu RZ, Wang Y, Vembar M, Jin ZY, Wang YN. Low Dose and Low Contrast Medium Coronary CT Angiography Using Dual-Layer Spectral Detector CT. *Int Heart J*. 2019 May 30;60(3):608-617. doi: 10.1536/ihj.18-340. PMID: 31105142.
 21. Yamak D, Pavlicek W, Boltz T, Panse PM, Frakes D, Akay M. Coronary calcium quantification using contrast-enhanced dual-energy computed tomography scans. *J Appl Clin Med Phys*. 2013 May 6;14(3):4014. doi: 10.1120/jacmp.v14i3.4014. PMID: 23652239; PMCID: PMC5714428.
 22. Mahoney R, Pavitt CW, Gordon D, Park B, Rubens MB, Nicol ED, Padley SP. Clinical validation of dual-source dual-energy computed tomography (DECT) for coronary and valve imaging in patients undergoing trans-catheter aortic valve

- implantation (TAVI). *Clin Radiol.* 2014 Aug;69(8):786-94. doi: 10.1016/j.crad.2014.03.010. PMID: 24842399.
23. Taylor AJ, Cerqueira M, Hodgson JM, Mark D, Min J, O'Gara P, Rubin GD; American College of Cardiology Foundation Appropriate Use Criteria Task Force; Society of Cardiovascular Computed Tomography; American College of Radiology; American Heart Association; American Society of Echocardiography; American Society of Nuclear Cardiology; North American Society for Cardiovascular Imaging; Society for Cardiovascular Angiography and Interventions; Society for Cardiovascular Magnetic Resonance. ACCF/SCCT/ACR/AHA/ASE/ASNC/NASCI/SCAI/SCMR 2010 Appropriate Use Criteria for Cardiac Computed Tomography. A Report of the American College of Cardiology Foundation Appropriate Use Criteria Task Force, the Society of Cardiovascular Computed Tomography, the American College of Radiology, the American Heart Association, the American Society of Echocardiography, the American Society of Nuclear Cardiology, the North American Society for Cardiovascular Imaging, the Society for Cardiovascular Angiography and Interventions, and the Society for Cardiovascular Magnetic Resonance. *J Cardiovasc Comput Tomogr.* 2010 Nov-Dec;4(6):407.e1-33. doi: 10.1016/j.jcct.2010.11.001. PMID: 21232696.
24. Ruzsics B, Lee H, Zwerner PL, Gebregziabher M, Costello P, Schoepf UJ. Dual-energy CT of the heart for diagnosing coronary artery stenosis and myocardial ischemia-initial experience. *Eur Radiol.* 2008 Nov;18(11):2414-24. doi: 10.1007/s00330-008-1022-x. PMID: 18523782.
25. Lenga L, Albrecht MH, Othman AE, Martin SS, Leithner D, D'Angelo T, Arendt C, Scholtz JE, De Cecco CN, Schoepf UJ, Vogl TJ, Wichmann JL. Monoenergetic

- Dual-energy Computed Tomographic Imaging: Cardiothoracic Applications. *J Thorac Imaging*. 2017 May;32(3):151-158. doi: 10.1097/RTI.0000000000000259. PMID: 28198752.
26. Grant KL, Flohr TG, Krauss B, Sedlmair M, Thomas C, Schmidt B. Assessment of an advanced image-based technique to calculate virtual monoenergetic computed tomographic images from a dual-energy examination to improve contrast-to-noise ratio in examinations using iodinated contrast media. *Invest Radiol*. 2014 Sep;49(9):586-92. doi: 10.1097/RLI.0000000000000060. PMID: 24710203.
 27. Marin D, Fananapazir G, Mileto A, Choudhury KR, Wilson JM, Nelson RC. Dual-energy multi-detector row CT with virtual monochromatic imaging for improving patient-to-patient uniformity of aortic enhancement during CT angiography: an in vitro and in vivo study. *Radiology*. 2014 Sep;272(3):895-902. doi: 10.1148/radiol.14132857. PMID: 24814182.
 28. Apfalter P, Sudarski S, Schneider D, Nance JW Jr, Haubenreisser H, Fink C, Schoenberg SO, Henzler T. Value of monoenergetic low-kV dual energy CT datasets for improved image quality of CT pulmonary angiography. *Eur J Radiol*. 2014 Feb;83(2):322-8. doi: 10.1016/j.ejrad.2013.11.005. PMID: 24361061.
 29. Sudarski S, Apfalter P, Nance JW Jr, Schneider D, Meyer M, Schoenberg SO, Fink C, Henzler T. Optimization of keV-settings in abdominal and lower extremity dual-source dual-energy CT angiography determined with virtual monoenergetic imaging. *Eur J Radiol*. 2013 Oct;82(10):e574-81. doi: 10.1016/j.ejrad.2013.04.040. PMID: 23763858.
 30. Leithner, D. et al. Evaluation of virtual monoenergetic imaging algorithms for dual-energy carotid and intracerebral CT angiography: Effects on image quality,

- artefacts and diagnostic performance for the detection of stenosis. *Eur. J. Radiol.* 99, 111–117 (2018).
31. Martin SS, Wichmann JL, Scholtz JE, Leithner D, D'Angelo T, Weyer H, Booz C, Lenga L, Vogl TJ, Albrecht MH. Noise-Optimized Virtual Monoenergetic Dual-Energy CT Improves Diagnostic Accuracy for the Detection of Active Arterial Bleeding of the Abdomen. *J Vasc Interv Radiol.* 2017 Sep;28(9):1257-1266. doi: 10.1016/j.jvir.2017.06.011. PMID: 28734847.
 32. Leithner D, Wichmann JL, Vogl TJ, Trommer J, Martin SS, Scholtz JE, Bodelle B, De Cecco CN, Duguay T, Nance JW Jr, Schoepf UJ, Albrecht MH. Virtual Monoenergetic Imaging and Iodine Perfusion Maps Improve Diagnostic Accuracy of Dual-Energy Computed Tomography Pulmonary Angiography With Suboptimal Contrast Attenuation. *Invest Radiol.* 2017 Nov;52(11):659-665. doi: 10.1097/RLI.0000000000000387. PMID: 28542094.
 33. Martin SS, Wichmann JL, Weyer H, Scholtz JE, Leithner D, Spandorfer A, Bodelle B, Jacobi V, Vogl TJ, Albrecht MH. Endoleaks after endovascular aortic aneurysm repair: Improved detection with noise-optimized virtual monoenergetic dual-energy CT. *Eur J Radiol.* 2017 Sep;94:125-132. doi: 10.1016/j.ejrad.2017.06.017. PMID: 28712695.
 34. Secchi F, De Cecco CN, Spearman JV, Silverman JR, Ebersberger U, Sardanelli F, Schoepf UJ. Monoenergetic extrapolation of cardiac dual energy CT for artifact reduction. *Acta Radiol.* 2015 Apr;56(4):413-8. doi: 10.1177/0284185114527867. PMID: 24615417.
 35. Stehli J, Clerc OF, Fuchs TA, Possner M, Gräni C, Benz DC, Buechel RR, Kaufmann PA. Impact of monochromatic coronary computed tomography angiography from single-source dual-energy CT on coronary stenosis

- quantification. *J Cardiovasc Comput Tomogr.* 2016 Mar-Apr;10(2):135-40. doi: 10.1016/j.jcct.2015.12.008. PMID: 26754621.
36. Symons R, Choi Y, Cork TE, Ahlman MA, Mallek M, Bluemke DA, Sandfort V. Optimized energy of spectral coronary CT angiography for coronary plaque detection and quantification. *J Cardiovasc Comput Tomogr.* 2018 Mar-Apr;12(2):108-114. doi: 10.1016/j.jcct.2018.01.006. PMID: 29397334.
37. Albrecht MH, Trommer J, Wichmann JL, Scholtz JE, Martin SS, Lehnert T, Vogl TJ, Bodelle B. Comprehensive Comparison of Virtual Monoenergetic and Linearly Blended Reconstruction Techniques in Third-Generation Dual-Source Dual-Energy Computed Tomography Angiography of the Thorax and Abdomen. *Invest Radiol.* 2016 Sep;51(9):582-90. doi: 10.1097/RLI.0000000000000272. PMID: 26953565.
38. D'Angelo T, Cicero G, Mazziotti S, Ascenti G, Albrecht MH, Martin SS, Othman AE, Vogl TJ, Wichmann JL. Dual energy computed tomography virtual monoenergetic imaging: technique and clinical applications. *Br J Radiol.* 2019 Jun;92(1098):20180546. doi: 10.1259/bjr.20180546. PMID: 30919651; PMCID: PMC6592074.
39. Delesalle, M.-A. et al. Spectral Optimization of Chest CT Angiography with Reduced Iodine Load: Experience in 80 Patients Evaluated with Dual-Source, Dual-Energy CT. *Radiology* 267, 256–266 (2013).
40. Carrascosa P, Capuñay C, Deviggiano A, Goldsmit A, Tajer C, Bettinotti M, Carrascosa J, Ivanc TB, Fallahi A, García MJ. Accuracy of low-dose prospectively gated axial coronary CT angiography for the assessment of coronary artery stenosis in patients with stable heart rate. *J Cardiovasc Comput Tomogr.* 2010 May-Jun;4(3):197-205. doi: 10.1016/j.jcct.2010.04.001. PMID: 20444666.

41. He J, Wang Q, Ma X, Sun Z. Dual-energy CT angiography of abdomen with routine concentration contrast agent in comparison with conventional single-energy CT with high concentration contrast agent. *Eur J Radiol.* 2015 Feb;84(2):221-7. doi: 10.1016/j.ejrad.2014.11.025. PMID: 25487820.
42. De Santis D, Caruso D, Schoepf UJ, Eid M, Albrecht MH, Duguay TM, Varga-Szemes A, Laghi A, De Cecco CN. Contrast media injection protocol optimization for dual-energy coronary CT angiography: results from a circulation phantom. *Eur Radiol.* 2018 Aug;28(8):3473-3481. doi: 10.1007/s00330-018-5308-3. PMID: 29488083.
43. Martin SS, Albrecht MH, Wichmann JL, Hüsters K, Scholtz JE, Booz C, Bodelle B, Bauer RW, Metzger SC, Vogl TJ, Lehnert T. Value of a noise-optimized virtual monoenergetic reconstruction technique in dual-energy CT for planning of transcatheter aortic valve replacement. *Eur Radiol.* 2017 Feb;27(2):705-714. doi: 10.1007/s00330-016-4422-3. PMID: 27236818.
44. Wichmann JL, Gillott MR, De Cecco CN, Mangold S, Varga-Szemes A, Yamada R, Otani K, Canstein C, Fuller SR, Vogl TJ, Todoran TM, Schoepf UJ. Dual-Energy Computed Tomography Angiography of the Lower Extremity Runoff: Impact of Noise-Optimized Virtual Monochromatic Imaging on Image Quality and Diagnostic Accuracy. *Invest Radiol.* 2016 Feb;51(2):139-46. doi: 10.1097/RLI.0000000000000216. PMID: 26561048.
45. D'Angelo T, Bucher AM, Lenga L, Arendt CT, Peterke JL, Caruso D, Mazziotti S, Blandino A, Ascenti G, Othman AE, Martin SS, Leithner D, Vogl TJ, Wichmann JL. Optimisation of window settings for traditional and noise-optimised virtual monoenergetic imaging in dual-energy computed tomography pulmonary

- angiography. *Eur Radiol.* 2018 Apr;28(4):1393-1401. doi: 10.1007/s00330-017-5059-6. PMID: 29018926.
46. Mangold S, Cannaó PM, Schoepf UJ, Wichmann JL, Canstein C, Fuller SR, Muscogiuri G, Varga-Szemes A, Nikolaou K, De Cecco CN. Impact of an advanced image-based monoenergetic reconstruction algorithm on coronary stent visualization using third generation dual-source dual-energy CT: a phantom study. *Eur Radiol.* 2016 Jun;26(6):1871-8. doi: 10.1007/s00330-015-3997-4. PMID: 26373752.
47. Hickethier T, Baeßler B, Kroeger JR, Doerner J, Pahn G, Maintz D, Michels G, Bunck AC. Monoenergetic reconstructions for imaging of coronary artery stents using spectral detector CT: In-vitro experience and comparison to conventional images. *J Cardiovasc Comput Tomogr.* 2017 Jan-Feb;11(1):33-39. doi: 10.1016/j.jcct.2016.12.005. PMID: 28096049.
48. Van Hedent S, Große Hokamp N, Kessner R, Gilkeson R, Ros PR, Gupta A. Effect of Virtual Monoenergetic Images From Spectral Detector Computed Tomography on Coronary Calcium Blooming. *J Comput Assist Tomogr.* 2018 Nov/Dec;42(6):912-918. doi: 10.1097/RCT.0000000000000811. PMID: 30371619.
49. De Santis D, Jin KN, Schoepf UJ, Grant KL, De Cecco CN, Nance JW Jr, Vogl TJ, Laghi A, Albrecht MH. Heavily Calcified Coronary Arteries: Advanced Calcium Subtraction Improves Luminal Visualization and Diagnostic Confidence in Dual-Energy Coronary Computed Tomography Angiography. *Invest Radiol.* 2018 Feb;53(2):103-109. doi: 10.1097/RLI.0000000000000416. PMID: 29016370.
50. Wichmann JL, Arbaciauskaite R, Kerl JM, Frellesen C, Bodelle B, Lehnert T, Monsefi N, Vogl TJ, Bauer RW. Evaluation of monoenergetic late iodine

- enhancement dual-energy computed tomography for imaging of chronic myocardial infarction. *Eur Radiol.* 2014 Jun;24(6):1211-8. doi: 10.1007/s00330-014-3126-9. PMID: 24599623.
51. Carrascosa P, Leipsic JA, Capunay C, Deviggiano A, Vallejos J, Goldsmit A, Rodriguez-Granillo GA. Monochromatic image reconstruction by dual energy imaging allows half iodine load computed tomography coronary angiography. *Eur J Radiol.* 2015 Oct;84(10):1915-20. doi: 10.1016/j.ejrad.2015.06.019. PMID: 26152868.
52. Leipsic J, Abbara S, Achenbach S, Cury R, Earls JP, Mancini GJ, Nieman K, Pontone G, Raff GL. SCCT guidelines for the interpretation and reporting of coronary CT angiography: a report of the Society of Cardiovascular Computed Tomography Guidelines Committee. *J Cardiovasc Comput Tomogr.* 2014 Sep-Oct;8(5):342-58. doi: 10.1016/j.jcct.2014.07.003. PMID: 25301040.
53. Rassouli N, Chalian H, Rajiah P, Dhanantwari A, Landeras L. Assessment of 70-keV virtual monoenergetic spectral images in abdominal CT imaging: A comparison study to conventional polychromatic 120-kVp images. *Abdom Radiol (NY).* 2017 Oct;42(10):2579-2586. doi: 10.1007/s00261-017-1151-2. PMID: 28421243.
54. Huang X, Gao S, Ma Y, Lu X, Jia Z, Hou Y. The optimal monoenergetic spectral image level of coronary computed tomography (CT) angiography on a dual-layer spectral detector CT with half-dose contrast media. *Quant Imaging Med Surg.* 2020 Mar;10(3):592-603. doi: 10.21037/qims.2020.02.17. PMID: 32269920; PMCID: PMC7136738.

55. Jin KN, De Cecco CN, Caruso D, Tesche C, Spandorfer A, Varga-Szemes A, Schoepf UJ. Myocardial perfusion imaging with dual energy CT. *Eur J Radiol.* 2016 Oct;85(10):1914-1921. doi: 10.1016/j.ejrad.2016.06.023. PMID: 2742741